A New Flexible Approach for Reconstructing Satellite-Based Land Surface Temperature Images
A Case Study With MODIS Data

Afsharipour, Seyedkarim; Jia, Li; Menenti, Massimo

DOI
10.1109/JSTARS.2025.3545404

Publication date
2025

Document Version
Final published version

Published in
IEEE Journal of Selected Topics in Applied Earth Observations and Remote Sensing

Citation (APA)
Afsharipour, S., Jia, L., & Menenti, M. (2025). A New Flexible Approach for Reconstructing Satellite-Based Land Surface Temperature Images: A Case Study With MODIS Data. *IEEE Journal of Selected Topics in Applied Earth Observations and Remote Sensing*, *18*, 7451-7467. https://doi.org/10.1109/JSTARS.2025.3545404

A New Flexible Approach for Reconstructing Satellite-Based Land Surface Temperature Images: A Case Study with MODIS Data

Seyedkarim Afsharipour, Li Jia, and Massimo Menenti

***Abstract*— Time-series of spatially continuous satellite data are increasingly used for environmental studies. Among these, land surface temperature (LST), retrieved from data such as the MODerate resolution Imaging Spectroradiometer (MODIS), plays a vital role in numerous applications. However, cloud cover significantly reduces the number of usable pixel-wise LST observations. Despite various documented methods for reconstructing missing LST pixels, challenges remain regarding their flexibility to handle varying gap percentages and reliance on multiple ancillary datasets. This study presents a flexible, and automated technique to reconstruct missing LST pixels without relying on ancillary data. The approach combines three innovative techniques: Global Regression Analysis (GRA), Local Regression Analyses (LRA), and Geo-spatial Analysis (GA). The Missing Pixels Percentage (MPP) of each day determines the appropriate technique to fill the gaps. The method was applied to daily Terra MODIS LST datasets (MOD11A1) at 1 km spatial resolution from 2002 to 2022. Two evaluation methods were conducted: comparing with in-situ measurements and introducing artificial gaps. The validation was demonstrated over the Heihe River basin in China and in four experimental areas worldwide with available ground measurements from FLUXNET. Validation with artificial gaps produced average Root Mean Square Error (RMSE) and Mean Absolute Error (MAE) of 2.33 K and 1.76 K, respectively. In-situ measurements indicated superior performance with R^2, RMSE, and MAE of 0.85, 4 K, and 3.4 K, outperforming two existing methods. The study demonstrates that the model accurately reconstructs missing pixels on heterogeneous surfaces under diverse conditions, effectively handling large datasets and complex gaps.**

This work was jointly funded by the project supported by the National Natural Science Foundation of China (NSFC) (Grant No. 42090014), the Chinese Academy of Sciences President's International Fellowship Initiative (Grant No. 2025PVA0200, 2020VTA0001), the MOST High-Level Foreign Expert Program (Grant No. G2022055010L), and the CAS-TWAS President's Fellowship Program. *(Corresponding author: Li Jia).*

Seyedkarim Afsharipour is with the National Key Laboratory of Remote Sensing and Digital Earth, Aerospace Information Research Institute, Chinese Academy of Sciences. Beijing 100101, China and also with University of Chinese Academy of Sciences, Beijing 100045, China (e-mail: seyedkarim@radi.ac.cn).

Li Jia is with the National Key Laboratory of Remote Sensing and Digital Earth, Aerospace Information Research Institute, Chinese Academy of Sciences. Beijing 100101, China (e-mail: jiali@aircas.ac.cn).

Massimo Menenti is with the Institute of Tibetan Plateau Research, Chinese Academy of Sciences, Beijing 100101, China, and National Key Laboratory of Remote Sensing and Digital Earth, Aerospace Information Research Institute, Chinese Academy of Sciences. Beijing 100101, China, and also with Faculty of Civil Engineering and Geosciences, Delft University of Technology, Delft, The Netherlands (e-mail: m.menenti@radi.ac.cn).

***Index Terms*— Land Surface Temperature (LST), Gap-filling, Spatio-temporal, MODIS**

I. INTRODUCTION

Time-series of spatially continuous satellite data at different spatial resolutions are being increasingly used for environmental studies [1], [2]. The Land Surface Temperature (LST) conveys critical information on the interactions between land and the atmosphere [3], [4], [5], [6]. Therefore, the study of LST, particularly of MODIS LST time series [7], [8], [9], is vital in numerous remote sensing applications, such as evapotranspiration estimation [10], [11], [12], [13], ecosystem drought monitoring [14], [15], [16], 17], crop mapping [18], [19], and soil moisture monitoring [20], [21], [22], [23]. However, cloud contamination significantly reduces the number of high quality LST retrievals. Such occurrences are more frequent during monsoons or in humid zones [3]. On average, about 60% of the MODIS LST retrievals are affected by cloud contamination [24]. This makes the reconstruction of the missing pixel values by gap-filling very relevant. According to the literature, the methods developed to fill the gaps in time-series of remote sensing data can be grouped as detailed below.

The first group is the spatial information-based methods, which use the information from other pixels of the same image to reconstruct missing pixels and fill the gaps. Weighted averaging is often employed to interpolate missing values, such as Kriging method [25], [26], [27]. In addition, image segmentation [28] and the novel neighborhood similar pixel interpolator [29] also use spatial interpolation to reconstruct missing values. Nevertheless, performance is particularly poor for heterogeneous surfaces and massive gaps [1], [30], [31]. The challenges with medium-resolution images stem from their inability to capture fine-scale spatial variability, which is critical for accurate interpolation across heterogeneous landscapes. As a result, these methods often yield visually blurred reconstructed images [3] and fail to provide reliable results when the spatial resolution is insufficient to represent the complexity of the terrain [31].

The second group is time-based methods, which reconstruct the missing values through temporal interpolation between different points in time [32], [33]. This group is widely used for high temporal resolution image data such as AVHRR and MODIS. For example, in a comprehensive study using temporal interpolation, Jönsson and Eklundh [34] developed the TIMESAT software package for analyzing time-series of satellite data. This package provides a number of built-in smoothing functions to model time series data and fill gaps. These include the Asymmetric Gaussian (AG), Double Logistic (DL), and Adaptive Savitzky-Golay (SG) methods. In addition, Gao, et al. [35] presented an algorithm based on the TIMESAT AG approach to reconstruct time series of MODIS Leaf Area Index (LAI retrievals). A robust regression algorithm was developed by Zeng, et al. [36], which uses multi-temporal information and identifies similar pixels under clear-sky conditions by applying a multi-temporal classification method. In terms of using full temporal time-series information, there are more reliable and complex methods in this category, such as the Temporal Fourier Analysis (TFA) and Temporal Harmonic Analysis (THA) [37]. These approaches [38], [39] have been implemented to reconstruct missing values and, at the same time, to extract information on signal components in numerous remote sensing data [33], [40], [41], [42], [43], [44], [45]. However, despite all the developments that have taken place, consecutive missing pixels are still a significant problem and lead to lower performance [46]. Studies have shown that methods such as temporal interpolation and harmonic analysis often struggle with consecutive missing pixels, leading to higher reconstruction errors and reduced data quality [47], [48].

Approaches that use both the spatial and temporal dimension of remotely sensed signals have been developed to reconstruct missing pixels in remote sensing data. This group is referred to as the spatio-temporal approaches, which address many of the drawbacks of the methods described above. Examples of such methods have been documented in literature [49], [50], [51], [52], [53], [54]. Accordingly, Pede and Mountrakis [55] compared the three types of approaches. Their results demonstrated that spatio-temporal methods performed better than either temporal or spatial interpolation in reconstructing the MODIS LST time series to remove gaps, even for severe gaps (more than 80 %). For spatio-temporal models, the general approach often starts with using the time-based methods for an initial approximation of missing pixels, which is then improved and refined by incorporating spatial models and auxiliary data. For instance, Zeng, et al. [56] introduced a two-step framework for reconstructing LST of satellite data that are often contaminated by clouds. The first step uses a multi-temporal reconstruction algorithm that fills in missing LST values by analyzing multiple LST images and using vegetation indices, like NDVI, to guide the process. This approach helps ensure that the recovered temperature values are accurate and reliable. In a second step, a surface energy balance equation-based procedure is used to correct these reconstructed LST values, taking into account the effect of clouds on shortwave irradiance data. However, the effectiveness of these methods is significantly influenced by the quality of the supporting data, such as radiation, vegetation, surface albedo, and atmospheric inputs. In another research, Shiff, et al. [57] presented a model for creating a worldwide continuous, gap-filled MODIS LST dataset. The method primarily involves combining satellite observations (i.e., MODIS LST) with modelled temperatures from the Climate Forecast System Version 2 (CFSv2). The TFA plays a crucial role in this process. It is used to derive the seasonal cycles (climatological temperatures) for each pixel based on MODIS LST and CFSv2 near-surface air temperatures. The method involves adding the CFSv2 temperature anomaly (deviation from the climatological mean temperature) to the climatological LST, thus filling the gaps in the data, particularly for periods of cloud cover when satellite data are not available. A notable limitation of this method is the reliance on auxiliary data with different spatial resolutions, such as 25 km for air temperature and 1 km for LST, which may affect the accuracy of the gap-filled data in spatially heterogeneous regions. Furthermore, through an extensive analysis of literature, particularly those focused on evaluating gap-filling algorithms [32], [40], [58], [60], it has been shown that despite the advantages associated with each approach, they are also accompanied by notable limitations. Although certain methods have high accuracy, they can be complex in terms of obtaining supplementary data and performing computations. For instance, Ravishankar, et al. [61] suggest that when the proportion of missing pixels is minimal, the use of interpolation techniques that rely on neighboring pixels can yield the most accurate outcomes. However, as the proportion of missing pixels increases, neighboring adjacent data becomes less representative, making techniques that incorporate supplementary data more effective [62], [63]. The presence of considerable temporal and spatial gaps can pose challenges in addressing this issue [1], [64]. Moreover, several existing approaches tend to require extensive computations to deal with significant gaps and large datasets [1].

To address aforementioned limitations, we propose a conditional, and flexible approach to tackle the challenges of reconstructing missing satellite data. This process starts with identifying gaps using quality flags and calculating the Missing Pixel Percentage (MPP) for each daily image. We then set objective thresholds based on the MPP deciles to guide the selection of spatial reconstruction techniques. Accordingly, if the MPP exceeds the maximum threshold, a method relying on global regression analysis, termed Global Regression Analysis (GRA) in this study, is used. For days where the MPP falls between the maximum and minimum thresholds, a technique based on local regression analysis, designated as Local Regression Analysis (LRA), is utilized. Finally, when the MPP is below the minimum threshold, a simple geospatial analysis, referred to here as Geo-spatial Analysis (GA), is employed.

The main features of the method are as follows: 1) it uses all the information provided by the spatial and temporal methods; 2) the choice of the reconstruction technique depends on the percentage of missing pixels observed on a given day; 3) the capability to properly handle various data gaps, even during periods with limited data availability; 4) a significant advantage of our method is its independence from auxiliary data. Unlike many other methods, our approach does not require any external or auxiliary datasets to fill the gaps; 5) the ability to perform fast computations by using parallel data processing.

The rest of the paper is structured as follows: Section II describes our methodology. Section III introduces the data and case studies. Section IV presents the results we achieved. Sections V and VI contain the discussion and conclusions, respectively.

II. METHODOLOGY

To reconstruct missing pixels in satellite data, particularly daily LST dataset, we have developed a flexible method. The main idea behind the method is derived from the fact that employing different methods to deal with gaps of various sizes can lead to better performance than using a single method [1], [65].

According to Fig. 1, our method involves several key steps: 1) Initially, gaps in the dataset (2002 to 2022) are identified using daily quality flags, and the MPP is calculated. 2) Based on the MPP frequency distribution, two thresholds, Min_{mpp} and Max_{mpp}, are established by taking the first and last deciles. These thresholds guide the selection of the reconstruction technique. 3) A reference year with a smooth temporal profile for each pixel is created by averaging the LST for each pixel from day 1 to day 365. Then any remaining gaps in this average year are filled through temporal interpolation or extrapolation, followed by applying TFA to generate a smooth temporal profile for each pixel (LST_{tfa}). 4) A specific year is chosen as the target year for analysis. 5) For each daily image in the selected target year, the MPP is compared to the established thresholds to determine the appropriate spatial reconstruction method. If the MPP exceeds Max_{mpp}, we use a reconstruction method called GRA based on constructing a regression equation between all pixels where both TFA estimates and observations are available. This regression is then applied to pixels where only TFA estimates are available to obtain the final reconstructed pixel values. When the MPP is between Min_{mpp} and Max_{mpp}, another reconstruction method called LRA method is used. This involves creating a local regression using a moving search window over each image, based on pixels with both TFA estimates and observations. The regression is then applied to pixels with only TFA estimates to obtain the final values. Finally, if the MPP is below Min_{mpp}, the GA method is employed, using data from neighboring pixels to reconstruct missing values for each image in the dataset.

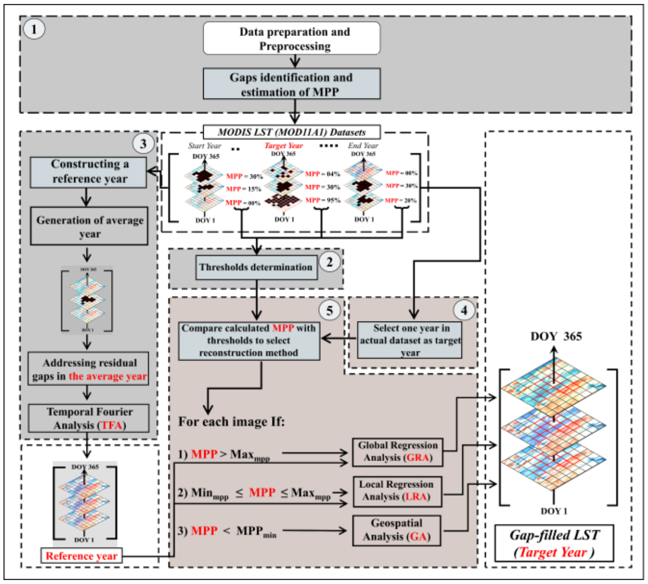

Fig. 1. Workflow of method. Each successive process is framed by a dashed line. A number at the top inside each frame specifies the order of execution of these processes. The gray color means that this process is done once for the entire dataset. Light brown indicates the process is repeated for different target years. Light blue represents the main outlined processes.

A. Gaps identification and MPP determination

This section first describes how abnormal pixels are identified and removed from the LST data, starting with the calculation of the MPP. We used the Quality Assurance (QA) information provided in the MODIS data. Through the QA flag, we successfully detected pixels degraded by the impact of clouds and other issues. Pixels were considered missing if the QA flags indicated problems such as "LST not produced due to cloud effects", "LST not produced primarily due to reasons other than cloud", "average emissivity error > 0.04" or "average LST error > 3 K". After identifying these missing pixels, we calculated the MPP for each day by dividing the number of missing pixels by the total number of pixels in the image (e.g., a study area). This step is crucial for guiding the selection of the appropriate reconstruction technique in the subsequent stages.

To effectively compare the MPP calculated for each day of the study period and to choose the proper missing pixel reconstruction method, it is crucial to establish two thresholds. These thresholds help us to determine the most suitable reconstruction technique based on the daily MPP. The approach described can be categorized as a conditional model, wherein the selection of the reconstruction method depends on the specific dataset. We denote these two thresholds as Min_{mpp} and Max_{mpp}. Instead of depending on user-defined values and visual inspections to set these thresholds, we propose using the first and last deciles of the MPP frequency distribution to establish Min_{mpp} and Max_{mpp}, respectively. Standardizing this process makes it easier to replicate the procedure across various studies and datasets. To determine these thresholds, we first calculate the daily MPP for the entire dataset, and then select the first and last deciles to establish Min_{mpp} and Max_{mpp}, respectively.

B. Constructing daily LST time series of a reference year

In this section, we detail the creation of a reference year, which serves as a foundational baseline for reconstructing missing pixels in our LST dataset.

1) Generation of daily LST time series of an average year:

In the first step, daily LST time series of an average year (denoted as LST_t) is constructed by averaging the valid LST data for each pixel across all available years from day 1 to day 365. To achieve a complete dataset, any remaining gaps in the average year were filled using the methods described in the following section.

After generating the average year, some pixels may still have missing LST values. To address these residual gaps, we employ temporal interpolation and extrapolation techniques. For gaps within the time series surrounded by valid data points, we use temporal interpolation. This method estimates missing values based on the trend and magnitude of the surrounding data. A commonly used approach is linear interpolation, which assumes a linear change between the nearest data points in the time series. The formula for linear interpolation is:

$$LST_{missing} = LST_{before} + \frac{LST_{before} - LST_{after}}{DoY_{before} - DoY_{after}} \times \left(DoY_{missing} - DoY_{befor} \right) \quad (1)$$

where $LST_{missing}$ is the estimated value for the missing data point, and LST_{before}, LST_{after} are the known LST values immediately before and after the missing data point, respectively.

In cases where missing values occur at the beginning or end of the time series, we utilize extrapolation to fill the remaining gaps. This involves extending a known data trend beyond the available observed data range to estimate the missing values. A simple linear extrapolation method is often used [66], which extends the trend observed in the nearest data points. The formula for linear extrapolation is similar to interpolation but applied to the range of outside of the available observed data. By filling these residual gaps, we ensure that the reference year dataset is comprehensive and ready for further use.

2) Smoothing of average year LST temporal profile by TFA:

In our methodology, TFA is utilized for each pixel in the average year dataset to construct the smoothed temporal profile for each pixel in the reference year. This approach is essential because each pixel exhibits unique temporal patterns for specific days of the year over multiple years, which often differ significantly from neighboring pixels, resulting in a lack of spatial continuity in the average image (day). By applying TFA to smooth the temporal profile, these inconsistencies are minimized, enhancing spatial continuity across the average image (day). TFA is a critical time-series analysis technique that effectively captures the seasonality of LST, as demonstrated in numerous previous studies (Menenti, et al. [33], Norzaida, et al. [67]; Scharlemann, et al. [68]. TFA decomposes an observed signal into a set of periodic components. A crucial requirement for the effective implementation of TFA, particularly when applying the Fast Fourier Transform (FFT), is the presence of uniformly spaced data points in time. This necessity is a cornerstone of numerous conventional TFA methodologies [69]. The constructed average year series (LST_{tfa}) in section C. 2 satisfies this requirement by providing a consistent and evenly distributed time series for each pixel. The outcome of the TFA procedure is a Fourier series representation (LST_{tfa}) of the processed time series (LST_t). As a result, the following equations define the Fourier series representation of (LST_{tfa}) [68]:

$$LST_{tfa} = \overline{LST} + \sum_{i=1}^{\frac{N}{2}-1} \left[a_i \cos\left(\frac{2\pi.i.t}{N} \right) + b_i \sin\left(\frac{2\pi.i.t}{N} \right) \right] \quad (2)$$

where the is the annual arithmetic mean of the daily LST_t time series of the average year of a pixel; N is the total number of observations (here as 365) of a time-series for a pixel; i is equal to (1, 2, … N/2-1); a_i and b_i are coefficients of the i^{th} harmonic. The component at a frequency ω_i = ($2\pi i$/365) is called the i^{th} harmonic, and for all i = N/2 these harmonics are written as:

$$a_i \cos(\omega_i t) + b_i \sin(\omega_i t) = R_i \cos(\omega_i t + \theta_i) \quad (3)$$

$$R_i = \sqrt{a_i^{\,2} + b_i^{\,2}} \ \text{ and } \ \theta_i = \tan^{-1}\left(-\frac{b_i}{a_i}\right) \quad (4)$$

where R_i and θ_i are the amplitude and phase of the i^{th} harmonic, respectively. FFT decomposes a time series into uncorrelated harmonics based on specific frequencies derived from the number of observations (N) and the length of the time series [70]. However, typically only a few harmonics significantly influence the total variance. Based on the findings of the studies by previous studies (Shiff, et al. [57]; Scharlemann, et al. [68]; Lensky and Dayan [71], we identified the significant components in our TFA of the MODIS data as having periods of four, six, and twelve months. Fig. 2 shows the two key parts of the previous equations to explain how LST_t is created and the way LST_{tfa} matches LST_t for a pixel in the Area 5 (Heihe river basin Fig.3). This figure demonstrates that LST_{tfa} aligns closely with the LST_t data, indicating that the three harmonics accurately represent the overall LST variation of the average year.

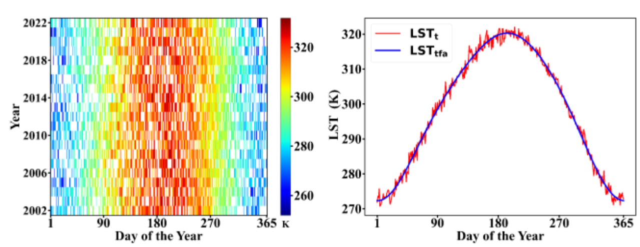

Fig 2. Demonstration for a pixel from Heihe river basin over years (2002-2022) for: Heatmap of LST values (left) (; LST time series of average year (LST_t) and smoothed profile of LST_t after TFA (LST_{tfa}) (right).

C. Reconstruction methods

We compare the calculated MPP of each daily image in the selected target year against the predetermined thresholds (sect

This article has been accepted for publication in IEEE Journal of Selected Topics in Applied Earth Observations and Remote Sensing. This is the author's version which has not been fully e
content may change prior to final publication. Citation information: DOI 10.1109/JSTARS.2025.3545404

II. B) to select the best reconstruction method for each image from 2002 to 2022. The reason for evaluating different reconstruction techniques lies in their varied strengths and weaknesses, making each one more appropriate for specific data and gap patterns [58], [60]. For images with MPP exceeding Max_{mpp}, indicating significant missing data, we use our GRA method to handle the extensive gaps. In cases where the MPP is below Min_{mpp}, suggesting minimal gaps, we apply our GA technique, which leverages data from neighboring pixels. For images where the MPP falls between these thresholds, we employ our LRA method, which combines temporal and spatial information to estimate the missing values. Using the MPP to select our method ensures that each image is reconstructed with the most appropriate technique. The following sections detail the GRA, LRA and GA methods.

1) Reconstruction using GRA:

In cases where the MPP is greater than the Max_{mpp} threshold, the GRA methodology is used. This method is particularly advantageous when techniques, such as local regression, are hindered by the scarcity of available data. The global linear regression model is fitted using all available valid (clear-sky) MODIS LST (LST_{mod}) observations on each date as predictand and the corresponding (same spatial position) reference year (LST_{tfa}) values as predictor. The regression model leverages these two datasets to establish the coefficients used for reconstruction. This regression is formulated as:

$$LST_{\mathrm{mod}}\left(P_{fGlobal},t\right)=a_g+b_g\times LST_{tfa}\left(P_{fGlobal},t\right) \tag{5}$$

where b_g and a_g are the slope and intercept of the global linear regression model fitted with values LST_{tfa} ($P_{fGlobal}$, t) and LST_{mod} ($P_{fGlobal}$, t) on a target date t, and subscript f means a set of valid observation in the study area. Once the coefficients a_g and b_g are defined, each missing pixel is reconstructed using (5) and the LST is estimated with TFA.

If MPP is 100% on a target day, the LST image is reconstructed using LST_{tfa}.

2) Reconstruction using GA:

According to Tobler [72], the First Law of Geography is that there is a spatial relationship between all entities, but the degree of relatedness is greater for closer entities than for more distant ones. The methodology employed in this paper to fill in missing pixels is based on this fundamental geographic notion. Visual examination of the images indicated that the use of neighborhood information and spatial analysis is a highly effective method of reconstructing missing data when the gap size is relatively small. This statement is consistent with Tobler's First Law, as it recognizes that the nearest pixels have a higher degree of correlation, hence allowing the use of neighborhood information to estimate missing values. To identify suitable reference pixels, the reference image (i.e., the LST_{tfa} image) on the same DoY (day of year) as the image to be processed (target image) was subjected to image segmentation [73]. The segmentation algorithm employed in this study was the K-means clustering algorithm [74], where the value of K was set to 5. The choice of K = 5 in the K-means clustering algorithm was primarily based on the existing literature [73], [74], that utilized this clustering method for gap-filling tasks. These studies suggested that the optimal value for K ranges between 3 and 7, a range proven to be effective for gap-filling applications. Therefore, we selected the average of this range as the constant value for K in this study. The K-means algorithm divides the image into K discrete clusters in the present scenario. By understanding the class of the target missing pixel, the 10 nearest (distance from the gap pixel) similar pixels in the same class as the target pixel were selected as effective pixels. Subsequently, the target missing pixels were reconstructed by a weighted average [75] using these effective pixels. The weights were assigned based on distance, with the nearest similar pixels receiving the highest weight.

3) Reconstruction using LRA:

This procedure is applied when the MPP is between the maximum and minimum thresholds. Initially, for a given missing pixel (target pixel) identified on the target day, an $n \times n$ window is created centered on the target pixel, with n being an odd number to ensure symmetry. Valid MODIS LST (LST_{mod}) values and values of corresponding pixels from LST_{tfa} in the $n \times n$ window is extracted. The LRA is applied when the number of valid pixels in the n × n window exceeds (n/2+0.5) to ensure a minimum number of valid data points for regression [76]. The regression model for valid pixels in each n × n window is shown below:

$$LST_{\mathrm{mod}}\left(P_{win1},t\right)=a_v+b_v\times LST_{tfa}\left(P_{win1},t\right) \tag{6}$$

where b_v and a_v are the slope and intercept of the linear regression model respectively, fitted by values between LST_{mod} (P_{winl}, t) and LST_{tfa} (P_{winl}, t) in a given search window, t is the target date. After obtaining the model outputs (a_v, b_v and R^2) and assessing the correlation of the data, the regression equation can be applied to reconstruct the missing pixel value using the LST_{tfa} of the corresponding pixel using (7). This is done when the coefficient of determination (R^2) exceeds a user-defined minimum correlation threshold (mincorrelation), set at 0.8 in this study. If the number of valid pixels or R^2 is insufficient, the window size is increased by two units (e.g., (n+2) × (n+2)) until the conditions are met or the window size is equal to the full image dimensions of the study region. If the LRA process fails to reconstruct the missing pixels at this stage, the GA is used to reconstruct the missing values of LST. This procedure is implemented across the entire image containing the missing pixels.

D. Validation method

The performance of the developed method was evaluated in two ways. The first was to artificially generate gaps, reconstruct them, and calculate the reconstruction error over the gap pixels. The second one was to evaluate the reconstruction of missing LST retrievals in various global conditions against in-situ LST measurements.

1) Evaluation using artificial gaps:

In this evaluation scenario all types of gaps were considered, both in terms of shape and size. In order to evaluate the effectiveness of the method, artificial gaps of varying sizes and shapes were created to reflect the actual gap patterns observed in the dataset. To illustrate the process of introducing a gap, consider the following example: assume that day t1 (Day of Year, DoY = t_1) is a cloud-free day (MPP = 0), and day t_2 has an MPP of 60%. To create artificial gaps that reflect actual conditions, the position (row, column) of missing pixels on day t_2 were used to eliminate pixels on day t_1. These artificial gaps on day t_1 were then filled using the developed method. Similarly, gaps with a MPP ranging from 5% to 100% were generated by artificially removing values from the selected clear days. The reconstructed pixels values were then compared with the actual values, and the errors were calculated. Note that the artificial gaps were created to cover a broad range of MPPs and temporal changes were considered by selecting different image dates for each season. Moreover, a comprehensive investigation of land use and land cover (LULC) was carried out. This investigation was crucial as it allowed us to evaluate the performance of our developed models across different LULC classes. By implementing this approach, it becomes possible to provide accurate assessments of the model effectiveness in specific LULC classes, enabling potential users to assess whether the model performance meets their specific needs and expectations.

2) Evaluation using ground measurements:

To evaluate the method performance in reconstructing missing pixels under natural cloudy conditions, in-situ LST measurements from FluxNet sites were used. The LST reconstructed values at each FluxNet station were extracted to calculate evaluation metrics by comparing them with actual observed LST.

To fully demonstrate the performance of the developed method, a comprehensive cross validation analysis was conducted to validate the newly developed model results by comparing it against two different models and datasets within the field of LST gap filling. The first model for comparison was developed by Shiff, et al. [57] (hereafter referred to as "Shiff2021 model"). This model utilizes TFA to analyze the seasonality of both LST and air temperature at 2m height. The core of Shiff2021 model methodology lies in using estimates of temperature anomalies to fill gaps in the LST data mainly resulted by cloud cover. This approach is particularly effective in integrating seasonal trends and actual air temperature variations to reconstruct missing LST data. The complete code for Shiff2021 model was made available and documented by Shiff, et al. [57] at GitHub (https://github.com/shilosh/ContinuousLST.git). The second model is based on a comprehensive dataset published by Zhang, et al. [77] (hereafter referred to as "Zhang2022 model"). This dataset represents a significant advancement in LST data, being derived from the MODIS 1 km resolution daily LST product. According to their study the first step is data preprocessing involves filtering low-quality pixels and filling gaps with LST values from three other observations on the same day. Then, the temporal trend of each pixel is modeled using a smoothing spline function, and the residuals between the observations and the trend are interpolated using neighboring pixels to estimate the missing values, which are reconstructed by adding these interpolated residuals to the overall temporal trend. The dataset extensive coverage and the novel approach in LST gap filling offer a solid basis for comparing the performance and effectiveness of our developed model.

3) Performance metrics:

We utilized mixed methods, including qualitative and quantitative analyses, to evaluate the proposed missing pixel reconstruction method. For the qualitative evaluation, we visually inspected the reconstructed images to identify any inconsistent patterns, spatial discontinuities or other anomalies that would indicate errors in the reconstruction process. For quantitative analysis, we calculated widely-used performance metrics for different reconstruction experiments to evaluate the method performance. These metrics included the coefficient of determination (R^2) value to assess the goodness of fit, Root Mean Square Error (RMSE) to evaluate the differences between the predicted and actual values, and Mean Absolute Error (MAE) to determine the absolute deviation between the predicted and actual values. The error metrics were calculated as:

$$R^2 = \frac{\left[\sum_{i=1}^{N}\left(S_i-\bar{S}\right).\left(O_i-\bar{O}\right)\right]}{\sum_{i=1}^{N}\left(S_i-\bar{S}\right)^2.\sum_{i=1}^{N}\left(O_i-\bar{O}\right)^2} \tag{7}$$

$$RMSE = \left[\frac{1}{N}\sum_{i=1}^{N}\left(O_i-\bar{S}\right)^2\right]^{\frac{1}{2}} \tag{8}$$

$$MAE = \frac{\left[\frac{1}{N}\sum_{i=1}^{N}\left(O_i-\bar{S}\right)^2\right]}{N} \tag{9}$$

where S_i is reconstructed value, is average reconstructed value, O_i is observed value, $\bar{O}$ is average observed value, N is number of data samples for evaluation.

III. Data and Study Areas

A. Satellite datasets

In term of method implementation this study used the MODIS LST daily product (MOD11A1 Version 6) at 1 km spatial resolution acquired by the Terra satellite (10:30 AM local time).

To evaluate the model's performance against in-situ LST measurements, we converted upwelling long-wave radiation data from FluxNet stations into LST. This conversion required emissivity estimates, which were derived using the Normalized Difference Vegetation Index (NDVI) and Leaf Area Index (LAI) based on red and Near Infrared (NIR) surface reflectance ((11) to (13)). We utilized daily red and NIR surface reflectance data from the MODIS (MCD43A4) product at a 500-meter resolution.

We downloaded the complete MODIS LST dataset (MOD11A1) and surface reflectance (MCD43A4) (Table I) using the Google Earth Engine (GEE) code editor environment. These datasets were then utilized to implement the proposed method in Python. Before downloading, all raster datasets were standardized to the same coordinate system and pixel size (1 km) using the GEE code editor.

TABLE I
DETAILED OVERVIEW OF THE MODIS DATA SETS USED IN THIS STUDY

Parameter	Data source	Period
LST	MOD11A1	2002 – 2022
Quality Assurance	MOD11A1-QA	2002 – 2022
Red Band NIR Band	MCD43A4.061	2012 – 2022
Land use / Land cover	MCD12Q1	2016 – 2021

B. Ground measurements for validation and experimental sites

In the present research, the developed model was evaluated against ground measurements from FLUXNET (https://fluxnet.org/data/) across various latitudes and under diverse weather circumstances. Sites from four experimental locations of FLUXNET were chosen for evaluation of the model performance, covering different land cover types (Fig. 3, Table II).

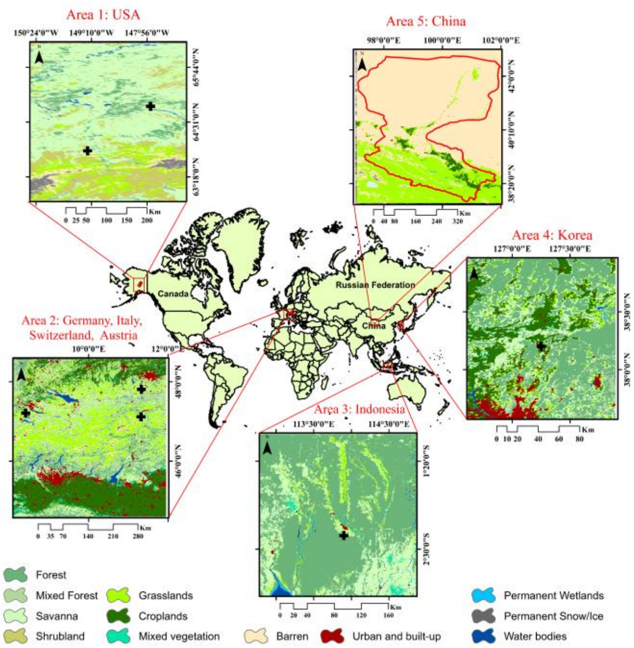

Fig. 3. Locations of ground experimental sites for model evaluation. The positions of ground sites are indicated by a black cross. The land cover classes are presented at bottom of figure.

TABLE II
DETAILED INFORMATION OF GROUND MEASUREMENTS DATA USED IN THIS STUDY

Area	Site ID/name	Country	Lat.	Long.	LULC	Years
Area 1	US-EML	USA	63.88	-149.25	Tundra	2015
	US-Uaf	USA	64.87	-147.85	Bog	2015
Area 2	AT-Neu	Austria	47.12	11.31	Alpine meadow	2010, 2012
	CH-Cha	Switzerland	47.21	8.41	Grassland	2012, 2013
	DE-SfN	Germany	47.81	11.33	Bog	2014
Area 3	ID-Pag	Indonesia	-2.32	113.9	Swamp	2017
Area 4	KR-CRK	Korea	38.20	127.25	Crop (Rice)	2015

Area 1 (including 2 FLUXNET sites) is situated in the western United States of America. The size of this test-area is approximately 71,000 km^2. Furthermore, the land cover within this region is predominantly characterized by the presence of snow and ice for the majority of the year. Area 2 (including 3 FLUXNET sites) is situated within various European countries, namely Germany, Switzerland, and Austria with the extent over 140,000 km2. Area 3 and 4 are located in Indonesia and South Korea, with areas of 40,000 and 15,000 km^2. Area 5, the Heihe River Basin in China, the Heihe River Basin (HRB), located between 96.5° E to 102.5° E longitude and 38.5° N to 43° N latitude, is the second largest inland river basin in China. This region is an arid and semi-arid environment, which makes it a notable subject of investigation for land surface process studies [78], [79], [80]. The Heihe River Basin can be divided into: the alpine region, which is characterized by a semi-arid climate and mainly consists of forests and grasslands; the midstream region, which is characterized by arid climate and is mainly used for crop cultivation with irrigation; and the downstream region, which is characterized by extreme arid climate and includes a large desert area. The HRB presents an ideal case study for LST gap-filling due to its ecological significance [81], diverse climate impacts, ongoing research into climate change effects [82], and practical applications in water resource management [83]. These factors collectively enhance the relevance and applicability of findings derived from studies conducted in this region.

The long-wave radiation (W/m^2) data from the sites of FLUXNET datasets (https://fluxnet.org/data/) and from the sites in Heihe river basin of China. To retrieve actual LST from the in-situ measurements of outgoing long-wave radiation flux (RL_{out}) and incoming long-wave radiation flux (RL_{in}) measured at a time close to the MODIS overpass, we inverted the Stefan-Boltzmann equation as:

$$LST = \sqrt[4]{\frac{RL_{out} - (1-\varepsilon_0)\times RL_{in}}{\varepsilon_0 \times \sigma}} \tag{10}$$

where ε_0 is the broad-band surface emissivity (dimensionless), σ is the Stefan-Boltzmann constant (5.67 × 10^{-8} W/m^2/K^4). The red and NIR bands from "MCD43A4.061" were used to calculate the broad-band surface emissivity based on the NDVI and the LAI [84] and performed for each day.

The broad-band surface emissivity (ε_0) is then determined using the LAI value as [85].

$$\varepsilon_0 = 0.95 + 0.01 \times LAI \ \text{ if } \ LAI < 3 \tag{11}$$

$$\varepsilon_0 = 0.98 \ \text{ when } \ LAI \geq 3 \tag{12}$$

We detected the presence of snow/ice and water as NDVI < 0 and we applied to such pixels (days) an emissivity value of ε_0=0.985 [86], [87]. LAI is derived from the NDVI as follows:

$$LAI = \frac{NDVI - NDVI_{\min}}{NDVI_{\max} - NDVI_{\min}} \tag{13}$$

In this equation, $NDVI_{min}$ and $NDVI_{max}$ are the minimum and maximum values of NDVI, respectively, over the period of observation, typically representing bare soil and dense vegetation. In many remote sensing studies, commonly adopted values for these parameters are 0.2 for $NDVI_{min}$ and 0.5 for $NDVI_{max}$, as they effectively characterize the spectral response of bare soil and dense vegetation, respectively [88], [89].

IV. RESULTS

A. Determining the MPP thresholds

The threshold determination of is a key step in the method implementation. We presented an example of this procedure

This article has been accepted for publication in IEEE Journal of Selected Topics in Applied Earth Observations and Remote Sensing. This is the author's version which has not been fully e
content may change prior to final publication. Citation information: DOI 10.1109/JSTARS.2025.3545404

for the HRB in Fig. 4. The result of thresholds calculation for the four experimental sites is presented in Fig. 5. For Area 1, these thresholds were found to be 4% and 88%, respectively. These values closely align with those obtained for the main site, as illustrated in Fig. 4. Areas 2 and 4 displayed similar values in their last deciles, but their first deciles varied significantly (approximately 15% for site 2 and around 2% for site 4). Site 3, however, presented a unique scenario due to its frequent cloud cover, resulting in first and last decile values of 51% and 96%, respectively. The significant differences observed necessitated careful calculation of thresholds for each site. For instance, the high MPP at Site 3 impairs the reliability of geospatial analysis. As a result, only GRA and LRA were applicable for this site. To establish consistent threshold values across all sites, the average values of first and last deciles were computed, and the standard deviation was subtracted from these averages to refine the thresholds. It is important to mention that extreme values (outliers) were excluded from the calculations of these averages. Hence, this method ultimately determined 7% and 89% as the thresholds for Min_{mpp} and Max_{mpp} respectively. For Site 3, this approach meant that the threshold for using the GA method (Min_{mpp}) was not utilized. Instead, the GRA and LRA methods were applied. Table III shows the minimum and maximum thresholds of missing data frequency between 2002 and 2022 in the five regions selected to evaluate the proposed method, as well as the averaged values of the thresholds.

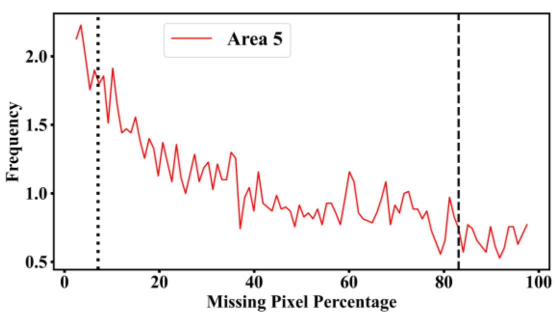

Fig 4. The Heihe river basin (Fig. 3) MPP frequency distribution of daily LST between 2002 and 2022: the right (dashed line) and left (dotted) line indicate the first and last deciles respectively, to establish the Min_{mpp} (dotted line) and Max_{mpp} (dashed line) thresholds.

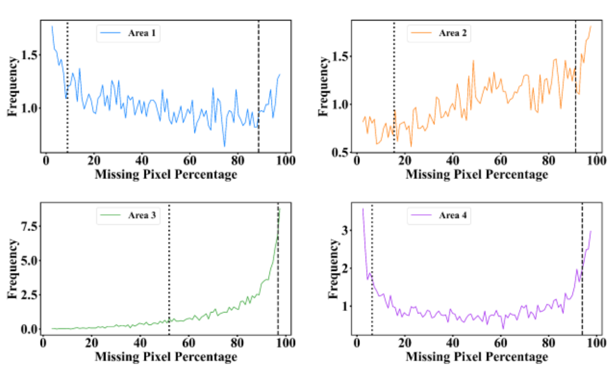

Fig. 5. The first (left lines) and last (right lines) decile values of the frequency distributions of MPP for different sites (see Fig. 4). The horizontal and vertical axis are the year and decile value, respectively.

TABLE III
SUMMARY OF MINIMUM AND MAXIMUM THRESHOLDS OF MISSING DATA FOR GAP-FILLING METHOD SELECTION IN THE STUDY AREAS

Study area (Site)	Min_{mpp}	Max_{mpp}	Method used
Heihe river basin	8%	83%	GA when MPP ≤ 7% LRA when 7% < MPP < 89% GRA when MPP ≥ 89%
Area 1	9%	88%	
Area 2	15%	93%	
Area 3	51%	96%	
Area 4	2%	95%	
Average	**7%** ± 3.8%	**89%** ± 2.9%	

B. Attributes of reconstructed pixels

Based on the results obtained from the Min_{mpp} and Max_{mpp} thresholds determination step (Sect IV.A), the relevant method (GA, LRA, and GRA) was selected to reconstruct the missing pixels. Consequently, missing pixels on days with MPP below 7% were reconstructed using the GA method. Missing pixels on days with MPP between 7% and 89% were reconstructed using the LRA technique. Similarly, missing pixels on days with MPP greater than 89% were reconstructed using the GRA method. As a result, this subsection discusses attributes of reconstructed images when the MPP falls within the determined Min_{mpp} and Max_{mpp} thresholds or exceeds the determined thresholds. The visual inspection concludes that the model output is visually acceptable (Fig. 6). There are no noticeable unconnected or crisp effects at the edges of missing pixels, even when a significant number of missing pixels are clustered together (e.g., 2021 (DoY = 309)). The three reconstruction methods used successfully handled the reconstruction of missing pixels within this range of MPP values. When the MPP was less than 7% (2017 (DoY = 057)), the reconstruction quality improved compared to cases with a higher proportion of missing data (98%). Our method was able to reconstruct the missing data with more valid pixels. Section C provides a quantitative evaluation of our reconstruction method is carried out by comparing it with in-situ ground measurements and by generating artificial gaps.

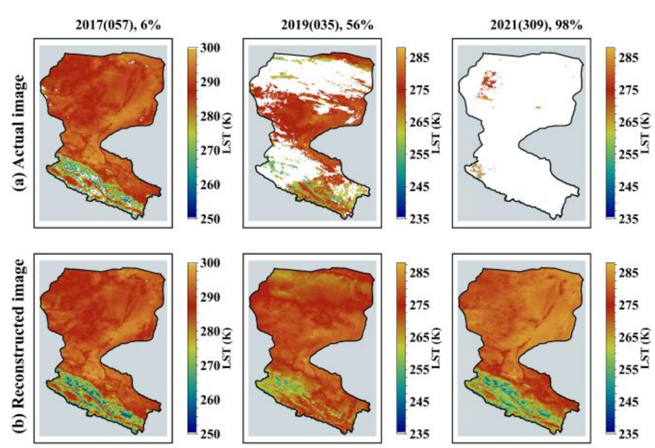

This article has been accepted for publication in IEEE Journal of Selected Topics in Applied Earth Observations and Remote Sensing. This is the author's version which has not been fully e
content may change prior to final publication. Citation information: DOI 10.1109/JSTARS.2025.3545404

Fig. 6. Actual images with different gap patterns (a) and reconstructed images (b) with MPP values varying between 6 and 98 % percent. At the top of each column: date of each image in the format of yyyy (DoY) and MPP value.

C. Method validation

1) Evaluation using ground measurements:
In this evaluation, performance metrics (section II.D.3) were calculated to assess the effectiveness of our model. The gap-filled results from the model were compared against in-situ measurements on days with missing data (gap days). Specifically, in-situ LST measurements from FluxNet stations, recorded at half-hourly intervals, were extracted to match the MODIS Terra overpass time (10:30 AM local time). For validation, reconstructed LST values corresponding to the FluxNet station locations were extracted only for the days when MODIS Terra pixels were missing due to clouds or other factors. Our method relies on available MODIS LST from clear-sky condition to estimate the missing LST observations due to clouds or other reasons, but it can capture the thermal memory of the surface, from both the temporal and spatial perspectives (our method used both temporal and spatial information to fill the gaps). Under significant temporal variability of cloud cover, the clear-sky MODIS observations would still capture a colder land surface due to the lower mean irradiance due to cloud cover during several days. This is also proved by the cases shown in Fig. 14 where the reconstructed LST on cloudy days is close to the in-situ observations under clouds. The comparisons served to evaluate the accuracy of the reconstructed LST against observed in-situ data. As an illustrative example, Fig. 7 presents scatter plots of our model results against in-situ LST measurements in Area 1. The comprehensive evaluation across all sites in the four areas listed in Table II is shown in Table IV. For comparative analysis, Table IV also includes the evaluation metrics of the Shiff2021 and Zhang2022 models, allowing for a cross-model performance assessment. The same validation process was applied to these models, ensuring a consistent basis for comparison.

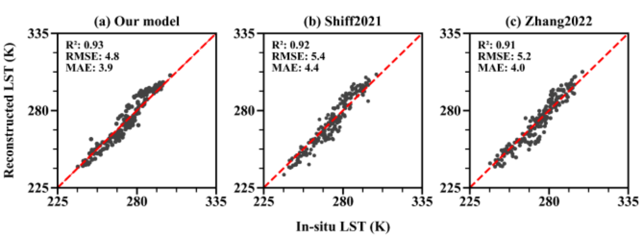

Fig. 7. Scatter plot comparing reconstructed LST with in-situ LST observations at 10:30 AM local time for Area 1. (a) Our model vs. in-situ measurements, (b) Shiff2021 model vs. in-situ measurements, and (c) Zhang2022 model vs. in-situ measurements. The performance metrics (R^2, RMSE, MAE) shown in each plot further document the accuracy of the reconstruction for each model.

TABLE IV

THE STATISTICAL METRICES OF COMPARISON BETWEEN THE GAP-FILLED LST BY OUR MODEL, SHIFF2021 MODEL AND ZHANG2022 MODEL WITH IN-SITU LST MEASUREMENTS FROM ALL SITES OF THE FOUR EXPERIMENT AREAS

Site No.	Our model			Shiff2021 model			Zhang2022 model		
	R^2	RMSE (K)	MAE (K)	R^2	RMSE (K)	MAE (K)	R^2	RMSE (K)	MAE (K)
Area 1	0.93	4.8	3.9	0.92	5.4	4.4	0.91	5.2	4.0
Area 2	0.8	4.47	3.59	0.67	5.61	4.5	0.8	4.49	3.54
Area 3	0.81	3.95	3.19	0.79	4.18	3.31	0.8	3.16	2.43
Area 4	0.89	3.64	2.77	0.88	3.79	2.95	0.85	4.29	3.49
Overall	0.85 ±0.05	4.05 ±0.4	3.4 ±0.4	0.81 ±0.09	4.7 ±0.7	3.7 ±0.6	0.83 ±0.04	4.9 ±0.7	3.9 ±0.5

The performance metrics were also evaluated for each site (Fig. 8). The three models had comparable and satisfactory R2 for all stations. Our method gave lower RMSE and MAE values for all sites. According to these results, the proposed method provides a satisfactory accuracy in the estimation of missing LST observations due to cloudy-sky conditions.

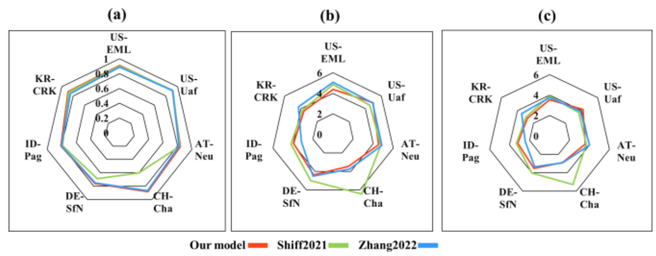

Fig. 8. Performance metrics of the three models for all FLUXNET sites: (a) R^2, (b) RMSE and (c) MAE.

Fig. 9 shows the examples of spatial maps of the reconstructed LST using our model, and the results from the Shiff2021 and Zhang2022 models for comparison, on different dates with different MPP conditions over the four areas with FLUXNET sites. This side-by-side comparison is important as it clearly shows the effectiveness of our model against two models and datasets in dealing with LST gaps. For Area 1 to Area 3 with an MPP from 39% to 73%, the LRA process in our method is used to reconstruct the missing pixels. For Area 4, the GRA in our method is used. Through pairwise comparisons, it is found that the values reconstructed by our method showed spatial consistency without any noticeable breaks. For example, in the case of 2017 for Areas 3 and 4, noticeable breaks are visible (highlighted black circle in Fig. 9) in the reconstructed LST maps by the other two models. This is an important demonstration of the ability of our model to produce reliable and coherent reconstructed images, which is essential for environmental monitoring and analysis.

This article has been accepted for publication in IEEE Journal of Selected Topics in Applied Earth Observations and Remote Sensing. This is the author's version which has not been fully e
content may change prior to final publication. Citation information: DOI 10.1109/JSTARS.2025.3545404

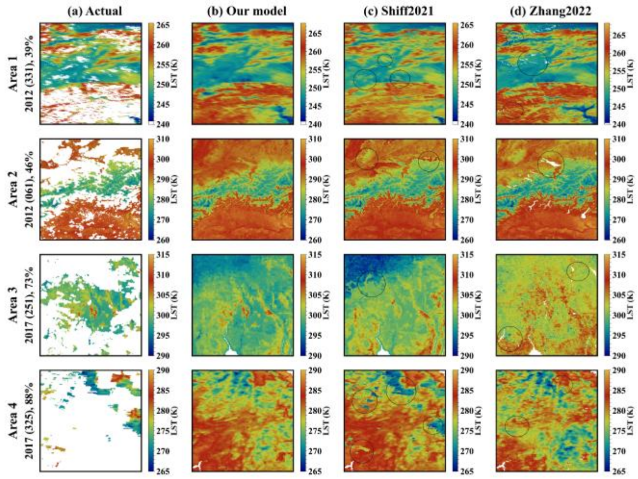

Fig. 9. Examples of missing pixel reconstruction under different MPP conditions over the four experimental Areas with FLUXNET sites. The first column (a) is the original MODIS LST image with gaps, the second column (b) is the image reconstructed by the developed method, the third and the fourth columns (c, d) are the LST images reconstructed by the Shiff2021 and Zhang2022 models. Each row represents a specific Area with MPP different values (row). The black circle highlights noticeable discontinuities between the reconstructed pixels and the original valid pixels.

2) Evaluation using artificial gaps:

To evaluate method performance in the reconstruction of missing pixels, we selected days with almost zero gaps over the region and use it as actual data (referred to as clear-day image). Then, artificial gaps with different patterns mimicking various scenarios of real-world conditions were created on these selected days by applying the shape and size of gaps from other images with higher MPP. The reconstruction accuracy was then evaluated by comparing the reconstructed pixel values in the artificial gap areas with those in the original clear-day image without gaps.

In total, 18 clear-day MODIS LST images between 2016 and 2021 in the Heihe river basin were selected and used to create gaps of different patterns, with MPP ranging from 4% to 96% (Table V). The results show the performance of our method in reconstructing missing pixel values. With the MPPs "≤" 7%, where the GA process was used, the lowest errors between the reconstructed and actual values were observed, as evidenced by the low RMSE (0.8 K – 1.7 K) and MAE (0.4 K – 1.0 K) values, indicating a good fit and minimal deviation from the actual values. With 7 < MPP < 89%, where the LRA process was used the method shows a higher RMSE (1.4 K – 3.1 K) and MAE (1.1 K – 2.1 K) than the GA results. With a mixed set of results where MPPs exceeded 89%, the GRA process was applied and the RMSE (3.2 K – 4.4 K) and MAE (2.4 K – 3.9 K) are increased.

TABLE IV

THE STATISTICAL METRICES OF COMPARISON BETWEEN THE RECONSTRUCTED AND THE ACTUAL LST VALUES ON SELECTED DATES FROM YEARS OF 2016 - 2021 FOR ARTIFICIAL GAPS

Year	(MPP ≤ 7%)				(7% < MPP < 89%)				(MPP > 89%)			
	DoY	MPP (%)	RMSE (K)	MAE (K)	DoY	MPP (%)	RMSE (K)	MAE (K)	DoY	MPP (%)	RMSE (K)	MAE (K)
2016	370	6	0.8	0.6	168	74	1.4	1.1	119	92	4.4	3.3
2017	277	7	1.3	1.0	187	44	2.0	1.4	285	96	3.2	2.7
2018	265	6	0.8	0.4	122	79	1.9	1.4	235	94	3.4	2.6
2019	211	6	1.3	1.0	240	62	1.9	1.3	222	90	3.3	2.7
2020	262	4	1.2	1.0	118	47	3.1	2.1	290	91	4.4	3.9
2021	253	7	1.7	1.0	070	33	2.4	1.5	127	96	3.2	2.4

Fig. 10 shows a representative example of the artificially introduced gaps and the reconstruction results using our method over the Heihe river basin. In this case, 62% spatial gaps were artificially introduced in the actual clear-day image (Fig. 10a), resulting in the gap-introduced image (Fig. 10b). The model was then used to reconstruct the missing pixels, resulting in the reconstructed image (Fig. 10c). As shown in Fig. 9, the reconstructed LST image is quite similar to the actual image and the reconstruction did not introduce noise and anomalies. Fig. 11 shows a scatter plot between the reconstructed and actual LST values within the gap region, further illustrating the performance of the model. The obtained RMSE of 1.9 K and MAE of 1.3 K indicate a low level of error, suggesting that our model effectively reconstructed the missing pixels while preserving the overall image quality.

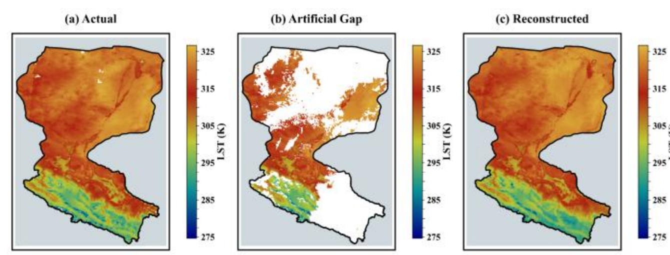

Fig. 10. Comparison of Actual (a), Artificial Gap (b), and Reconstructed (c) LST images from year 2019, DoY = 240 with MPP of 62%.

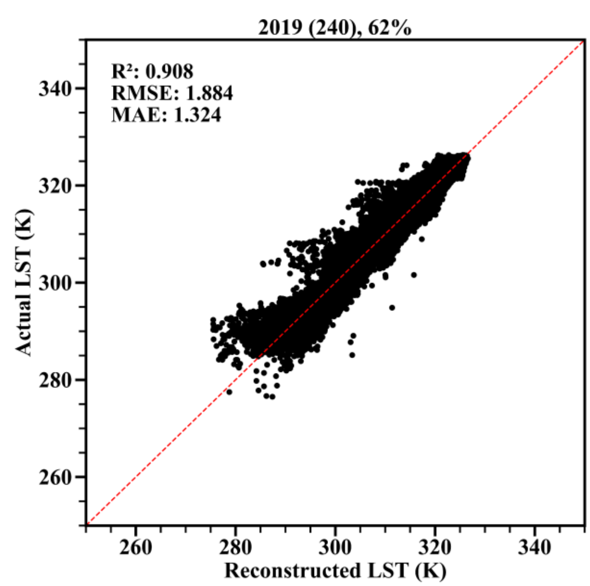

This article has been accepted for publication in IEEE Journal of Selected Topics in Applied Earth Observations and Remote Sensing. This is the author's version which has not been fully e
content may change prior to final publication. Citation information: DOI 10.1109/JSTARS.2025.3545404

Fig. 11. Scatter plots of reconstructed and actual LST values on DoY 240 in 2019 with MPP of 62% in the Heihe river basin.

To summarize the model performance in different MPP conditions, the values of performance metrics were averaged for four MPP bins (Fig.12). The lowest error rate was achieved in the bin MPP< 30% with RMSE of 1.5 K and MAE 1.2 K. In the bin 60% < MPP< 90% we found RMSE = 2.5 K and MAE = 1.9 K, while in the bin MPP > 90% RMSE = 3.8 K and MAE = 3.2 K.

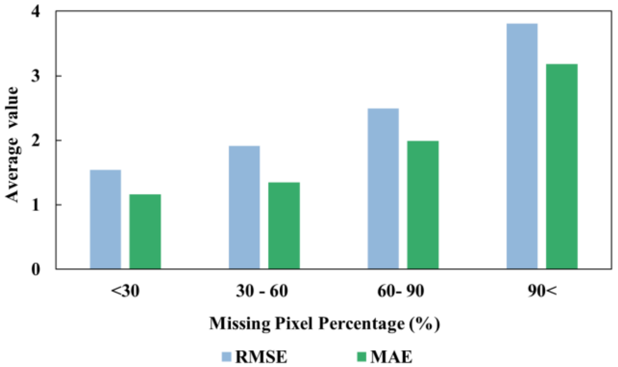

Fig. 12. Mean values of reconstruction error metrics in selected MPP bins on the selected dates from years of 2016 - 2021.

An additional validation technique was implemented to evaluate the model accuracy across various LULC classes (Table VI). The class labeled "Barren" exhibited the highest R^2 of 0.90, which can be attributed to bared area is more homogeneous when comparing with other classes in the HRB.

Furthermore, it is worth noting that the pixels classified as Urban and Built-up Lands exhibited the lowest R^2, i.e. 0.70, with mean R^2 across all classes being 0.80. The pixels labeled "Permanent Snow and Ice" had a substantial difference in LST compared to the surrounding pixels. This discrepancy resulted in the highest recorded RMSE at 3.16 K and MAE at 2.2 K. The classes "Water Bodies" and "Permanent Wetlands" had the lowest values of RMSE of 1.0 K and 1.1 K, and MAE of 1.0 K and 0.9 K, respectively.

Moreover, it should be emphasized that croplands had the largest number of missing pixels after barren lands and the RMSE and MAE were 1.9 K and 1.5 K, respectively. Thus, the developed method had a satisfactory performance in reconstructing missing LST across various LULC classes (Table VI).

TABLE VI

ERROR METRICS OF RECONSTRUCTED LST BY LULC

LULC Class Name	R^2 (-)	RMSE (K)	MAE (K)
Barren	0.90	2.2	1.9
Croplands	0.78	1.9	1.5
Urban and Built-up Lands	0.70	2.5	2.2
Permanent Snow and Ice	0.80	3.2	2.2
Permanent Wetlands	0.82	1.1	0.9
Evergreen Needle leaf Forests	0.85	1.6	1.3
Grasslands	0.86	3.0	2.4
Water Bodies	0.73	1.0	1.0
Savannas	0.71	2.5	2.4

V. DISCUSSION

1) The determination of MPP thresholds and evaluation of reconstructed pixels:

The determination of the Min_{mpp} and Max_{mpp} thresholds is a key aspect of the proposed method, as highlighted in Section A. As explained in Fig. 4 and Fig .5, the adoption of 7% and 89% as the MPP thresholds is supported by the underlying statistics, as it is necessary to establish consistent values (section VI. A) for the thresholds across all sites. This choice emphasized the importance of establishing clear and consistent thresholds for effective model implementation and helped to standardize and automate the model execution.

The differences in the MPP frequency distribution across sites are significant (Fig. 13), suggesting that the contribution of each of the three gap-filling algorithms varies across sites. The LRA method contributed the most to the reconstruction of missing pixels in all sites, while the GA method was approximately the least involved in most sites (the contribution of GA was zero in site 3). The contribution of the GRA method in site 3 was significant due to high MPPs.

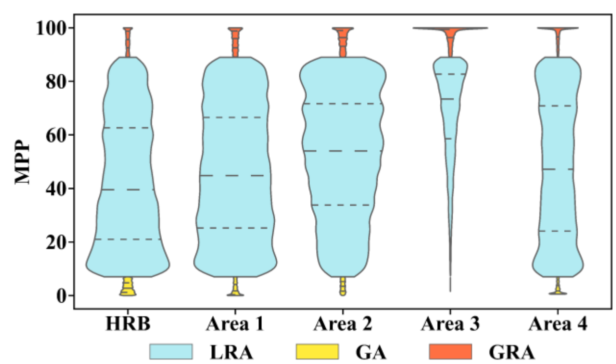

Fig. 13. The violin plot for MPP distribution (y axes) across different sites (x axes). The hue value is set as different method contribution to reconstructing missing pixels with three different colors (yellow, green and red colors are related to methods LRA, GA and GRA, respectively).

Section B investigated the characteristics of the reconstructed missing pixels, emphasizing the impact of the predetermined MPP thresholds. It examines how the application of different processes - GA, LRA, and GRA - contributes to the model adaptability in reconstructing pixels, given the established

This article has been accepted for publication in IEEE Journal of Selected Topics in Applied Earth Observations and Remote Sensing. This is the author's version which has not been fully e
content may change prior to final publication. Citation information: DOI 10.1109/JSTARS.2025.3545404

MPP threshold ranges, ensuring visual coherence and consistency across the dataset.

Analyzing the attributes of the reconstructed pixels shows that the method provides visual coherence and seamless transitions in the reconstructed images. The LRA technique, which handles the reconstruction of missing pixels when the MPP is between the high and low thresholds, plays a vital role, as highlighted by research that suggests the effectiveness of regression models in spatial data analysis due to their ability to clarify relationships between spatially correlated variables [90]. The absence of noticeable breaks at the edges of missing pixels, even when many missing pixels clustered together (Fig. 6, DoY 309 in 2021), confirms the robustness of the method. Nevertheless, it is crucial to acknowledge the existence of slight visual inconsistencies that can be detected at the edges between pre-existing pixels and reconstructed pixels, particularly when dealing with images in the mid-range of MPP (Fig. 6, DoY 035 in 2019). This is due to the fundamental difference in temperature between the missing, often cooler, cloud-covered pixels and cloud-free observations of LST. The role of clouds in influencing LST is well-documented, affecting the at-surface radiation balance and resulting in cooler temperatures [91]. The model effectively reconstructs missing pixels with limited data. Our model effectiveness is particularly noticeable when dealing with large gaps, where the MPP reaches almost 100%. To better illustrate the process and the reconstructed results, we have included a time series of the reconstructed LST for one pixel from each of the five experimental areas (Fig. 14) Figure 14 highlights the severe data gaps in some areas, such as Area 1 and Area 3, where, no valid LST observations were available on certain days due to cloud cover or other factors. Figure 14 demonstrates how our model has effectively reconstructed the missing pixels and captured the daily LST fluctuation by leveraging the valid clear-sky MODIS LST observations surrounding the gap pixel through the spatial regression analyses, i.e. GRA, LRA and GA, used in our method, and the periodic trends captured by the reference year time series. Figure 14 visually supports the robustness of our model in reconstructing missing LST values, even in areas with significant data gaps, while closely matching in-situ observed LST trends. Our approach ensures that the reconstructed missing LST data maintains continuity and reflects realistic temperature variations, which is critical for accurate environmental monitoring and analysis [66], [92]. The ability to accurately reconstruct missing data, particularly in cases of high MPP, is a significant advance in remote sensing data analysis, as it enhances the utility of the MODIS dataset for long-term climate studies and environmental monitoring [93].

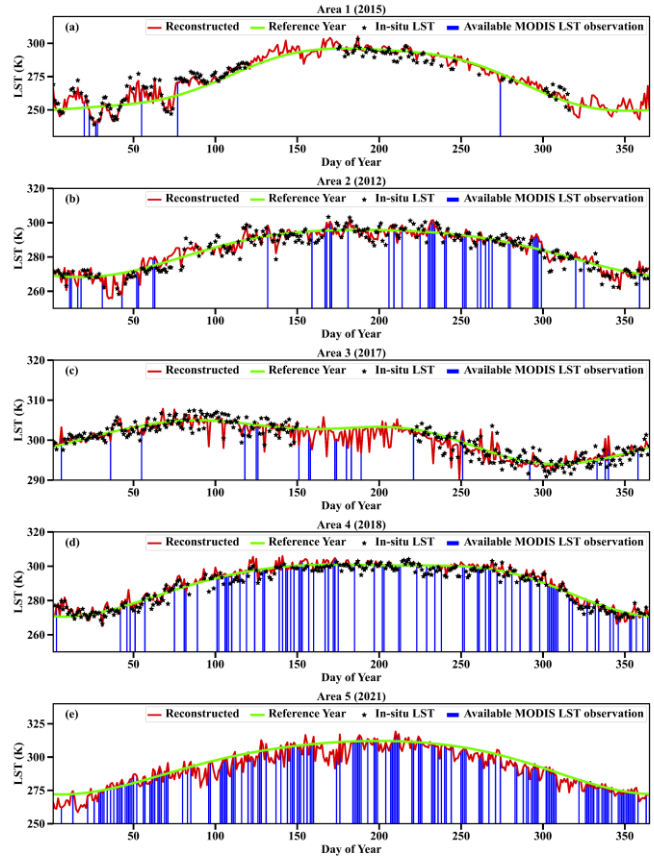

Fig. 14. Timeseries of reconstructed and reference year LST values of a random pixel taken from each one of the four experimental Areas over one year (Area 1: 2015; Area 2: 2017; Area 3: 2018; Area 4: 2021). White spaces between the blue bars are the gaps that we reconstructed using our model.

2) Model Validation and Performance

The validation results underscore the model reliability in reconstructing LST images over a range of MPP. Validation by applying artificial gaps was essential to document its effectiveness, a method frequently used in prior studies. For instance, Weiss, et al. [94] utilized artificial gaps in strip form to validate their model accuracy, achieving an R^2 of over 0.87 and an RMSE of approximately 2.5 K. Other studies, such as Siabi, et al. [1] and Yao, et al. [95], validated their models using square-shaped artificial gaps. Notwithstanding the results thus far, the utilization of systematic artificial gaps, such as striped or square patterns, fails to depict real-world conditions accurately. Consequently, this study employed artificial gaps of varying sizes derived from actual cloud cover conditions to address this limitation. Based on the data shown in Fig. 12, the RMSE was approximately 2.1 K. Also, the results document a consistent model performance, marked by a $R^2 = 0.90$ between reconstructed and actual data, irrespective of the MPP magnitude. The reliability of reconstructed data, shown by this correlation, underscores the model adaptability across a wide MPP range. These findings align with previous studies emphasizing the importance of a high degree of correlation for ensuring reliable model predictions [96]. As regards the MPP impact, there was a notable variation in RMSE, and MAE values across the MPP range, indicating the model adaptability to the extent and pattern of gaps. For example, the increase in RMSE and MAE with higher MPP (Fig. 12) emphasizes the inherent challenges associated with reconstructing images with extensive gaps, a finding consistent with previous literature [97], [98].

The investigation across various LULC classes has deepened our understanding of the model flexibility and adaptability. Notably, the highest R^2 value was observed in the 'Barren' class, while it was the lowest in 'Urban and Built-up Lands'. These results highlight the complexity of temporal variability across distinct land cover types, which can amplify the challenges in temporal sampling and the reconstruction of missing pixels, particularly in dynamic urban areas. This observation is consistent with previous research underscoring the impact of LULC variability on the accuracy of the LST reconstruction models [99]. The differences in RMSE and MAE values across different LULC classes, especially the higher values in "Permanent Snow and Ice" on the high altitude and steep slope mountainous areas with complex topography. Also, gap-filling methods are less effective in rugged terrain where mixed pixels (areas containing both snow and other elements such as rock or vegetation) are common. These mixed pixels, predominant at the MODIS resolution, complicate accurate reconstruction of missing pixels [100], [101], [102]. Therefore, these complexities in mountain terrain, including aspects such as steep terrain and severe climatic conditions, inherently challenge the reconstruction of missing pixels and highlight the role of LULC characteristics in determining reconstruction accuracy. The low RMSE and MAE values in "Water Bodies" and "Permanent Wetlands" indicate temporal stability in these classes, confirming previous research findings on the limited temporal variability in the of LST of water bodies [7], [103]. The satisfactory performance of the method in reconstructing the LST of arable lands, especially croplands with a considerable number of missing pixels, is extremely important, given the criticality of accurate LST data in agricultural applications and food security studies [104].

Previous Section (VI. C) focused on the performance of the methodology in the presence of natural cloudy conditions, a crucial and realistic aspect of any satellite-derived data analysis. Cloud cover can significantly obscure or distort observations of LST, hence understanding the model performance under such conditions is necessary for its broader applicability. We evaluated the method performance using in-situ LST radiometric measurements at FLUXNET sites as ground truth [24], [105], [106]. This enhanced the practical relevance of our evaluation.

The successful reconstruction of missing pixels by our model, even in areas with occasionally high MPP values, is consistent with findings from other studies, emphasizing the importance of accurate missing data reconstruction [107]. The challenge of missing data due to clouds is a well-documented obstacle in global LST datasets. The ability of our method to handle large gaps without introducing visible discontinuities suggests a promising application to remote sensing data, where cloud cover and technical issues often result in incomplete data. Our method compared favorably with two other methods and datasets (Fig. 9). Our method gave a consistent reconstruction across various sites and MPP values, while both methods of Shiff2021 and Zhang2022 displayed inconsistencies. It can be inferred that our method captures local variability in LST better than either Shiff2021 model and Zhang2022 model [108]. The statistical analyses further support this observation. R^2 values indicate that both models provide accurate and reliable reconstructions of in-situ LST data. However, with a mean R^2 of 0.85, the primary model slightly outperforms the models of Shiff2021 and Zhang2022, which gave a mean R^2 of 0.81 (see Fig. 8). In some cases (Table IV) the R^2 values were comparable for the three methods, but our method consistently gave lower RMSE and MAE (Table IV).

3) Advantages and limitations of the proposed method

According to the results presented, the current model has three notable features that distinguish it. Firstly, it demonstrates a strong ability to perform satisfactorily despite data scarcity. For instance, popular machine learning models [106], [109], [110], [111], [112], [113], [114], rely heavily on the abundance of valid data and suffer degraded performance under high MPP conditions or under frequent cloud cover, whereas our model performs well. The approach of averaging temperature values and reconstructing missing values in these averages through temporal linear interpolation, prior to applying Fourier analysis has equipped our model to perform reliably even when data is sparse. This is clearly illustrated in Fig. 14 (Area 3), with additional support from Figs. 6, 9 and 11, which confirms the model robust performance of the model in such challenging conditions. Secondly, our model uniquely operates without the need for ancillary data to reconstruct missing pixels. This is in contrasts to most models that rely on ancillary data [110], [115], [116], [117], [118], [119], which increase complexity, processing time and data volume, although sometime improving accuracy. In addition, differences in resolution or scale between ancillary datasets and LST data can introduce errors, particularly in heterogeneous landscapes. For example, when Shiff2021 model uses air temperature data at a 25 km resolution, it mismatches the finer 1 km resolution of MODIS LST data. Our model avoids these problems by exploiting a novel method and the inherent dimensions of the available data, effectively negating the need for ancillary inputs and still delivering satisfactory performance. Thus, the conditional nature of our model and its independence from ancillary data make it a simple, yet effective solution applicable to different global regions, as demonstrated and thoroughly evaluated in our test sites.

Despite its promising capabilities in reconstructing missing LST pixels, our model has limitations. For example, the theory that clearly distinguishes between clear- and cloudy-conditions in determining LST is not completely considered in this study. In contrast, the methods developed by Zheng et al. [57] and Shiff et al. [120] utilize either energy balance or air temperature to differentiate these conditions. Another example of our method limitation, its effectiveness is somewhat reduced in heterogeneous landscapes, such as mountainous areas with rugged topography and steep slopes. This could potentially limit the applicability of the model in such environments. Furthermore, in cases where missing pixels are due to localized phenomena not captured by these neighboring pixels, such as a fire event, the reconstruction based on these neighbors may not reflect the true condition. This indicates a limitation in the model ability to handle isolated events within the target pixel that are not characteristic of the surrounding area.

VI. Conclusion

In this study, we developed a gap-filling model using different reconstruction techniques, namely GRA, LRA, and GA, each designed for specific MPP ranges. The practical significance of the approach was documented by an in-depth evaluation, largely based on the application of artificial gaps. This method revealed valuable capabilities in improving LST spatial and temporal completeness. The GA, used for low MPP situations, demonstrated exceptional accuracy, with the lowest RMSE and MAE indicating high accuracy. The LRA, applied in moderate MPP ranges, showed strong performance with a noticeable increase in RMSE and MAE compared to GA. At high MPP, the GRA displayed varied performance, reflecting the inherent challenges of dealing with less available information in datasets with extensive missing pixels. Despite these complexities, the model generally exhibited excellent capability in handling the entire range of MPP, adapting to varying data conditions and maintaining a satisfactory accuracy and reliability under challenging circumstances. Additionally, the method achieved a satisfactory performance across different LULC classes, with varying levels of reconstruction accuracy reflected in the applied metrics. In terms of cross validation and model comparison despite the respectable performance of Shiff2021 and Zhang2022, our method outperformed them, since it achieved lower RMSE and MAE across different test sites, highlighting its superior efficiency in dealing with datasets with extensive gaps. The method evaluation emphasized the capability to perform efficiently in diverse situations. Further studies are expected to apply this method in environmental research to better identify limitations and propose targeted improvements.

The proposed method can generate daily daytime LST datasets with complete spatial and temporal coverage, which allows an extensive and detailed analysis of LST variability. This approach and the resulting high-quality reconstructions are crucial for understanding and interpreting the variability and trend in LST, a vital variable in climatological studies, offering insights into climate changes and land-atmosphere interactions.

Acknowledgment:

The authors would like to thank the reviewers and editors for their valuable comments.

References

[1] N. Siabi, S. H. Sanaeinejad, and B. Ghahraman, “Effective method for filling gaps in time series of environmental remote sensing data: An example on evapotranspiration and land surface temperature images,” *Comput. Electron. Agric.*, vol. 193, p. 106619, Feb. 2022.

[2] X. Zhang et al., "Reconstruction of all-weather land surface temperature based on a combined physical and data-driven model," (in eng), *Environ Sci Pollut Res Int*, vol. 30, no. 32, pp. 78865-78878, Jul 2023, doi: 10.1007/s11356-023-27986-z.

[3] W. Yu, J. Tan, M. Ma, X. Li, X. She, and Z. Song, “An effective similar-pixel reconstruction of the high-frequency cloud-covered areas of Southwest China,” *Remote Sens. (Basel)*, vol. 11, no. 3, p. 336, 2019.

[4] A. Dai, J. C. Fyfe, S.-P. Xie, and X. Dai, “Decadal modulation of global surface temperature by internal climate variability,” *Nat. Clim. Chang.*, vol. 5, no. 6, pp. 555–559, 2015.

[5] M. Anderson, W. P. Kustas, J. M. Norman, C. R. Hain, J. R. Mecikalski, L. Schultz, et al., “Mapping daily evapotranspiration at field to global scales using geostationary and polar orbiting satellite imagery,” Hydrol. Earth Syst. Sci. Discuss., vol. 7, pp. 5957–5990, 2010.

[6] Y. Gong, H. Li, H. Shen, C. Meng, and P. Wu, “Cloud-covered MODIS LST reconstruction by combining assimilation data and remote sensing data through a nonlocality-reinforced network,” Int. J. Appl. Earth Obs. Geoinf., vol. 117, p. 103195, Mar. 2023.

[7] Z. Wu, H. Teng, H. Chen, L. Han, and L. Chen, “Reconstruction of Gap-Free Land Surface Temperature at a 100 m Spatial Resolution from Multidimensional Data: A Case in Wuhan, China,” *Sensors (Basel)*, vol. 23, no. 2, p. 913, Jan. 12 2023.,

[8] W. Zhao, H. Wu, G. Yin, and S.-B. Duan, “Normalization of the temporal effect on the MODIS land surface temperature product using random forest regression,” *ISPRS J. Photogramm. Remote Sens.*, vol. 152, pp. 109–118, Jun. 2019.

[9] G. Hulley, S. Shivers, E. Wetherley, and R. Cudd, "New ECOSTRESS and MODIS Land Surface Temperature Data Reveal Fine-Scale Heat Vulnerability in Cities: A Case Study for Los Angeles County, California," *Remote Sensing*, vol. 11, no. 18, p. 2136, 2019, doi: https://doi.org/10.3390/rs11182136.

[10] Y. Jiang and Q. Weng, “Estimation of hourly and daily evapotranspiration and soil moisture using downscaled LST over various urban surfaces,” *GIsci. Remote Sens.*, vol. 54, no. 1, pp. 95–117, 2017.

[11] P. Hao, L. Di, and L. Guo, “Estimation of crop evapotranspiration from MODIS data by combining random forest and trapezoidal models,” *Agric. Water Manage.*, vol. 259, p. 107249, 2022.

[12] H. Awada, S. Di Prima, C. Sirca, F. Giadrossich, S. Marras, D. Spano, *et al.*, “A remote sensing and modeling integrated approach for constructing continuous time series of daily actual evapotranspiration,” *Agric. Water Manage.*, vol. 260, p. 107320, 2022.

[13] A. Allies, A. Olioso, B. Cappelaere, G. Boulet, J. Etchanchu, H. Barral, *et al.*, “A remote sensing data fusion method for continuous daily evapotranspiration mapping at kilometric scale in Sahelian areas,” *J. Hydrol. (Amst.)*, vol. 607, p. 127504, 2022.

[14] G. Dall’Olmo and A. Karnieli, “Monitoring phenological cycles of desert ecosystems using NDVI and LST data derived from NOAA-AVHRR imagery,” *Int. J. Remote Sens.*, vol. 23, no. 19, pp. 4055–4071, 2002.

[15] P. Sandeep, G. P. Obi Reddy, R. Jegankumar, and K. C. Arun Kumar, "Monitoring of agricultural drought in semi-arid ecosystem of Peninsular India through indices derived from time-series CHIRPS and MODIS datasets," *Ecological Indicators*, vol. 121, p. 107033, 2021/02/01/ 2021, doi: https://doi.org/10.1016/j.ecolind.2020.107033.

[16] F. Xie and H. Fan, “Deriving drought indices from MODIS vegetation indices (NDVI/EVI) and Land Surface Temperature (LST): Is data reconstruction necessary?” *Int. J. Appl. Earth Obs. Geoinf.*, vol. 101, p. 102352, 2021.

[17] S. Muster, M. Langer, A. Abnizova, K. L. Young, and J. Boike, “Spatio-temporal sensitivity of MODIS land surface temperature anomalies indicates high potential for large-scale land cover change detection in Arctic permafrost landscapes,” *Remote Sens. Environ.*, vol. 168, pp. 1–12, 2015.

[18] G. Zhang, X. Xiao, J. Dong, W. Kou, C. Jin, Y. Qin, *et al.*, “Mapping paddy rice planting areas through time series analysis of MODIS land surface temperature and vegetation index data,” *ISPRS J. Photogramm. Remote Sens.*, vol. 106, pp. 157–171, Aug. 2015.

[19] J. Chang, M. C. Hansen, K. Pittman, M. Carroll, and C. DiMiceli, “Corn and soybean mapping in the United States using MODIS time-series data sets,” *Agron. J.*, vol. 99, no. 6, pp. 1654–1664, 2007.

[20] P. K. Srivastava, D. Han, M. R. Ramirez, and T. Islam, "Machine learning techniques for downscaling SMOS satellite soil moisture using MODIS land surface temperature for hydrological application," *Water Resour. Manage.*, vol. 27, no. 8, pp. 3127–3144, 2013.

[21] L. Wang, J. Qu, S. Zhang, X. Hao, and S. Dasgupta, "Soil moisture estimation using MODIS and ground measurements in eastern China," *Int. J. Remote Sens.*, vol. 28, no. 6, pp. 1413–1418, 2007.

[22] W. Zhao, F. Wen, Q. Wang, N. Sanchez, and M. Piles, "Seamless downscaling of the ESA CCI soil moisture data at the daily scale with MODIS land products," *J. Hydrol. (Amst.)*, vol. 603, p. 126930, 2021.

[23] P. Song, Y. Zhang, J. Guo, J. Shi, T. Zhao, and B. Tong, *A 1-km daily surface soil moisture dataset of enhanced coverage under all-weather conditions over China in 2003–2019*. Earth System Science Data Discussions, 2022, pp. 1–51.

[24] S.-B. Duan, Z.-L. Li, and P. Leng, "A framework for the retrieval of all-weather land surface temperature at a high spatial resolution from polar-orbiting thermal infrared and passive microwave data," *Remote Sens. Environ.*, vol. 195, pp. 107–117, 2017.

[25] E. Kostopoulou, "Applicability of ordinary Kriging modeling techniques for filling satellite data gaps in support of coastal management," *Model. Earth Syst. Environ.*, vol. 7, no. 2, pp. 1145–1158, 2021.

[26] E. Addink and A. Stein, "A comparison of conventional and geostatistical methods to replace clouded pixels in NOAA-AVHRR images," *Int. J. Remote Sens.*, vol. 20, no. 5, pp. 961–977, 1999.

[27] R. E. Rossi, J. L. Dungan, and L. R. Beck, "Kriging in the shadows: Geostatistical interpolation for remote sensing," *Remote Sens. Environ.*, vol. 49, no. 1, pp. 32–40, 1994.

[28] S. K. Maxwell, G. L. Schmidt, and J. C. Storey, "A multi-scale segmentation approach to filling gaps in Landsat ETM+ SLC-off images," *Int. J. Remote Sens.*, vol. 28, no. 23, pp. 5339–5356, 2007, doi: 10.1080/01431160601034902.

[29] J. Chen, X. Zhu, J. E. Vogelmann, F. Gao, and S. Jin, "A simple and effective method for filling gaps in Landsat ETM+ SLC-off images," *Remote Sens. Environ.*, vol. 115, no. 4, pp. 1053–1064, 2011.

[30] W. Hu, M. Li, Y. Liu, Q. Huang, and K. Mao, "A new method of restoring ETM+ SLC-off images based on multi-temporal images," in *2011 19th International Conference on Geoinformatics*, 24-26 June 2011 2011, pp. 1-4, doi: 10.1109/GeoInformatics.2011.5981182.

[31] Q. Wang, Y. Tang, X. Tong, and P. M. Atkinson, "Filling gaps in cloudy Landsat LST product by spatial-temporal fusion of multi-scale data," *Remote Sensing of Environment*, vol. 306, p. 114142, 2024/05/15/ 2024, doi: https://doi.org/10.1016/j.rse.2024.114142.

[32] Y. Julien and J. A. Sobrino, "Comparison of cloud-reconstruction methods for time series of composite NDVI data," *Remote Sens. Environ.*, vol. 114, no. 3, pp. 618–625, 2010.

[33] M. Menenti, S. Azzali, W. Verhoef, and R. van Swol, "Mapping agroecological zones and time lag in vegetation growth by means of fourier analysis of time series of NDVI images," *Advances in Space Research*, vol. 13, no. 5, pp. 233-237, 1993/05/01/ 1993, doi: https://doi.org/10.1016/0273-1177(93)90550-U.

[34] P. Jönsson and L. Eklundh, "TIMESAT—A program for analyzing time-series of satellite sensor data," *Comput. Geosci.*, vol. 30, no. 8, pp. 833–845, 2004.

[35] F. Gao, J. T. Morisette, R. E. Wolfe, G. Ederer, J. Pedelty, E. Masuoka, et al., "An algorithm to produce temporally and spatially continuous MODIS-LAI time series," IEEE Geosci. Remote Sens. Lett., vol. 5, no. 1, pp. 60–64, 2008.

[36] C. Zeng, H. Shen, M. Zhong, L. Zhang, and P. Wu, "Reconstructing MODIS LST Based on Multitemporal Classification and Robust Regression," IEEE Geoscience and Remote Sensing Letters, vol. 12, no. 3, pp. 512-516, 2015, doi: 10.1109/LGRS.2014.2348651.

[37] S. Azzali and M. Menenti, Fourier analysis of temporal NDVI in the Southern African and American continents. Netherlands Remote Sensing Board. BCRS, 1996.

[38] M. Menenti, L. Jia, and Z.-L. Li, "Multi-angular thermal infrared observations of terrestrial vegetation," Advances in Land Remote Sensing: System. Modeling, Inversion and Application, 2008, pp. 51–93.

[39] M. Menenti, H. G. Malamiri, H. Shang, S. M. Alfieri, C. Maffei, and L. Jia, "Observing the response of terrestrial vegetation to climate variability across a range of time scales by time series analysis of land surface temperature," *Multitemporal Remote Sensing: Methods and Applications,* pp. 277-315, 2016.

[40] J. Zhou, L. Jia, and M. Menenti, "Reconstruction of global MODIS NDVI time series: Performance of Harmonic ANalysis of Time Series (HANTS)," *Remote Sens. Environ.*, vol. 163, pp. 217–228, 2015.

[41] G. Roerink, M. Menenti, and W. Verhoef, "Reconstructing cloudfree NDVI composites using Fourier analysis of time series," *Int. J. Remote Sens.*, vol. 21, no. 9, pp. 1911–1917, 2000.

[42] X. Jiang, D. Wang, L. Tang, J. Hu, and X. Xi, "Analysing the vegetation cover variation of China from AVHRR-NDVI data," *Int. J. Remote Sens.*, vol. 29, no. 17-18, pp. 5301–5311, 2008.

[43] L. Zeng, B. D. Wardlow, S. Hu, X. Zhang, G. Zhou, G. Peng, *et al.*, "A novel strategy to reconstruct NDVI time-series with high temporal resolution from MODIS multi-temporal composite products," *Remote Sens. (Basel)*, vol. 13, no. 7, p. 1397, 2021.

[44] H. Lecomte, S. Rosat, and M. Mandea, "Gap filling between GRACE and GRACE-FO missions: assessment of interpolation techniques," *Journal of Geodesy*, vol. 98, no. 12, p. 107, 2024/11/23 2024, doi: 10.1007/s00190-024-01917-3.

[45] S. Azzali and M. Menenti, "Mapping vegetation-soil-climate complexes in southern Africa using temporal Fourier analysis of NOAA-AVHRR NDVI data," *International Journal of Remote Sensing*, vol. 21, no. 5, pp. 973-996, 2000/01/01 2000, doi: 10.1080/014311600210380.

[46] [46] Y. Wang, X. Zhou, Z. Ao, K. Xiao, C. Yan, and Q. Xin, "Gap-Filling and Missing Information Recovery for Time Series of MODIS Data Using Deep Learning-Based Methods," *Remote Sensing*, vol. 14, no. 19, p. 4692, 2022.

[47] Q. Liu *et al.*, "A Spatiotemporally Constrained Interpolation Method for Missing Pixel Values in the Suomi-NPP VIIRS Monthly Composite Images: Taking Shanghai as an Example," *Remote Sensing*, vol. 15, no. 9, p. 2480, 2023.

[48] Z. Tang, G. Amatulli, P. K. E. Pellikka, and J. Heiskanen, "Spectral Temporal Information for Missing Data Reconstruction (STIMDR) of Landsat Reflectance Time Series," *Remote Sensing*, vol. 14, no. 1, p. 172, 2022. [Online]. Available: https://www.mdpi.com/2072-4292/14/1/172.

[49] S. Kang, S. W. Running, M. Zhao, J. S. Kimball, and J. Glassy, "Improving continuity of MODIS terrestrial photosynthesis products using an interpolation scheme for cloudy pixels," *Int. J. Remote Sens.*, vol. 26, no. 8, pp. 1659–1676, 2005.

[50] P. Yu *et al.*, "Global spatiotemporally continuous MODIS land surface temperature dataset," *Scientific Data*, vol. 9, no. 1, p. 143, 2022/04/01 2022, doi: 10.1038/s41597-022-01214-8.

[51] L. Poggio, A. Gimona, and I. Brown, "Spatio-temporal MODIS EVI gap filling under cloud cover: An example in Scotland," *ISPRS J. Photogramm. Remote Sens.*, vol. 72, pp. 56–72, 2012.

[52] [52] L. Yan and D. P. Roy, "Large-area gap filling of Landsat reflectance time series by spectral-angle-mapper based spatio-temporal similarity (SAMSTS)," *Remote Sens. (Basel)*, vol. 10, no. 4, p. 609, 2018.

[53] F. Gerber, R. de Jong, M. E. Schaepman, G. Schaepman-Strub, and R. Furrer, "Predicting missing values in spatio-temporal remote sensing data," *IEEE Trans. Geosci. Remote Sens.*, vol. 56, no. 5, pp. 2841–2853, 2018.

[54] A. F. Þórðarson, A. Baum, M. García, S. M. Vicente-Serrano, and A. Stockmarr, "Gap-Filling of NDVI Satellite Data Using

Tucker Decomposition: Exploiting Spatio-Temporal Patterns," *Remote Sens. (Basel)*, vol. 13, no. 19, p. 4007, 2021.

[55] T. Pede and G. Mountrakis, "An empirical comparison of interpolation methods for MODIS 8-day land surface temperature composites across the conterminous Unites States," *ISPRS J. Photogramm. Remote Sens.*, vol. 142, pp. 137–150, 2018.

[56] C. Zeng, D. Long, H. Shen, P. Wu, Y. Cui, and Y. Hong, "A two-step framework for reconstructing remotely sensed land surface temperatures contaminated by cloud," *ISPRS J. Photogramm. Remote Sens.*, vol. 141, pp. 30–45, 2018.

[57] S. Shiff, D. Helman, and I. M. Lensky, "Worldwide continuous gap-filled MODIS land surface temperature dataset," *Sci. Data*, vol. 8, no. 1, p. 74, Mar. 4 2021.

[58] [58] C. Fagandini, V. Todaro, M. G. Tanda, J. L. Pereira, L. Azevedo, and A. Zanini, "Missing Rainfall Daily Data: A Comparison Among Gap-Filling Approaches," *Mathematical Geosciences*, vol. 56, no. 2, pp. 191-217, 2024/02/01 2024, doi: 10.1007/s11004-023-10078-6.

[59] R. Liu, R. Shang, Y. Liu, and X. Lu, "Global evaluation of gap-filling approaches for seasonal NDVI with considering vegetation growth trajectory, protection of key point, noise resistance and curve stability," *Remote Sensing of Environment*, vol. 189, pp. 164-179, 2017/02/01/ 2017, doi: : https://doi.org/10.1016/j.rse.2016.11.023.

[60] N. Siabi, S. H. Sanaeinejad, and B. Ghahraman, "Comprehensive evaluation of a spatio-temporal gap filling algorithm: Using remotely sensed precipitation, LST and ET data," *Journal of Environmental Management*, vol. 261, p. 110228, 2020/05/01/ 2020, doi: https://doi.org/10.1016/j.jenvman.2020.110228.

[61] S. Ravishankar, J. C. Ye, and J. A. Fessler, "Image Reconstruction: From Sparsity to Data-Adaptive Methods and Machine Learning," *Proceedings of the IEEE*, vol. 108, no. 1, pp. 86-109, 2020, doi: 10.1109/JPROC.2019.2936204.

[62] S. C. Gustafson, G. R. Little, J. S. Loomis, and T. S. Puterbaugh, "Optimal reconstruction of missing-pixel images," *Appl. Opt.*, vol. 31, no. 32, pp. 6829-6830, 1992/11/10 1992, doi: 10.1364/AO.31.006829.

[63] M. Chen, Z. Sun, B. H. Newell, C. A. Corr, and W. Gao, "Missing Pixel Reconstruction on Landsat 8 Analysis Ready Data Land Surface Temperature Image Patches Using Source-Augmented Partial Convolution," *Remote Sensing*, vol. 12, no. 19, p. 3143, 2020.

[64] J. Xiao, A. K. Aggarwal, N. H. Duc, A. Arya, U. K. Rage, and R. Avtar, "A review of remote sensing image spatiotemporal fusion: Challenges, applications and recent trends," *Remote Sensing Applications: Society and Environment*, vol. 32, p. 101005, 2023/11/01/ 2023, doi: https://doi.org/10.1016/j.rsase.2023.101005.

[65] S. Kandasamy, F. Baret, A. Verger, P. Neveux, and M. Weiss, "A comparison of methods for smoothing and gap filling time series of remote sensing observations–application to MODIS LAI products," *Biogeosciences*, vol. 10, no. 6, pp. 4055–4071, 2013.

[66] D. Chen, Q. Zhuang, L. Zhu, and W. Zhang, "Comparison of methods for reconstructing MODIS land surface temperature under cloudy conditions," Appl. Sci. (Basel), vol. 12, no. 12, p. 6068, 2022.

[67] A. Norzaida, M. D. Zalina, and Y. Fadhilah, "Application of Fourier series in managing the seasonality of convective and monsoon rainfall," Hydrological Sciences Journal, vol. 61, no. 10, pp. 1967-1980, 2016/07/26 2016, doi: 10.1080/02626667.2015.1062892.

[68] J. P. W. Scharlemann, D. Benz, S. I. Hay, B. V. Purse, A. J. Tatem, G. R. Wint, et al., "Global data for ecology and epidemiology: A novel algorithm for temporal Fourier processing MODIS data," PLoS One, vol. 3, no. 1, p. e1408, Jan. 9 2008.

[69] W. H. Press, S. A. Teukolsky, W. T. Vetterling, and B. P. Flannery, *FORTRAN numerical recipes*. Cambridge University Press, 1997.

[70] C. Tipton, "Basics of Fourier Analysis of Time Series Data: A practical guide to use of the Fourier transform in an industrial setting," *Johns. Matthey Technol. Rev.*, vol. 66, no. 2, pp. 169–176, 2022.

[71] I. M. Lensky and U. Dayan, "Detection of finescale climatic features from satellites and implications for agricultural planning," *Bull. Am. Meteorol. Soc.*, vol. 92, no. 9, pp. 1131–1136, 2011.

[72] W. Tobler, "On the first law of geography: A reply," *Ann. Assoc. Am. Geogr.*, vol. 94, no. 2, pp. 304–310, 2004.

[73] Y. Luo, K. Guan, and J. Peng, "STAIR: A generic and fully-automated method to fuse multiple sources of optical satellite data to generate a high-resolution, daily and cloud-/gap-free surface reflectance product," *Remote Sensing of Environment*, vol. 214, pp. 87-99, 2018/09/01/ 2018, doi: https://doi.org/10.1016/j.rse.2018.04.042.

[74] [74] M. Ahmed, R. Seraj, and S. M. S. Islam, "The k-means Algorithm: A Comprehensive Survey and Performance Evaluation," *Electronics*, vol. 9, no. 8, p. 1295, 2020.

[75] T. Chen et al., "A Methodological Approach for Gap Filling of WFV Gaofen-1 Images from Spatial Autocorrelation and Enhanced Weighting," *Atmosphere*, vol. 15, no. 3, p. 252, 2024.

[76] A. O. Sykes, "An introduction to regression analysis," 1993.

[77] T. Zhang, Y. Zhou, Z. Zhu, X. Li, and G. R. Asrar, "A global seamless 1 km resolution daily land surface temperature dataset (2003–2020)," *Earth Syst. Sci*. Data, vol. 14, no. 2, pp. 651-664, 2022, doi: 10.5194/essd-14-651-2022.

[78] Y. Cui, L. Song, and W. Fan, "Generation of spatio-temporally continuous evapotranspiration and its components by coupling a two-source energy balance model and a deep neural network over the Heihe River Basin," *Journal of Hydrology*, vol. 597, p. 126176, 2021/06/01/ 2021, doi: https://doi.org/10.1016/j.jhydrol.2021.126176.

[79] N. Yan, W. Zhu, X. Feng, and S. Chang, "Spatial-temporal change analysis of evapotranspiration in the Heihe River Basin," in *2014 Third International Workshop on Earth Observation and Remote Sensing Applications (EORSA)*, 11-14 June 2014 2014, pp. 38-41, doi: 10.1109/EORSA.2014.6927845.

[80] L. Jia, H. Shang, and M. Menenti, "Vegetation response to upstream water yield in the Heihe river by time series analysis of MODIS data," *Hydrol. Earth Syst. Sci. Discuss.*, vol. 7, pp. 4177–4218, 2010.

[81] W. Geng, X. Jiang, Y. Lei, J. Zhang, and H. Zhao, "The Allocation of Water Resources in the Midstream of Heihe River for the "97 Water Diversion Scheme" and the "Three Red Lines"," *Int. J. Environ. Res. Public Health*, vol. 18, no. 4, p. 1887, Feb. 16 2021.,

[82] K. Luo, F. Tao, J. P. Moiwo, and D. Xiao, "Attribution of hydrological change in Heihe River Basin to climate and land use change in the past three decades," *Scientific Reports*, vol. 6, no. 1, p. 33704, 2016/09/20 2016, doi: 10.1038/srep33704.

[83] Z. Li, W. Li, Z. Li, and X. Lv, "Responses of Runoff and Its Extremes to Climate Change in the Upper Catchment of the Heihe River Basin, China," Atmosphere, vol. 14, no. 3, p. 539, 2023.

[84] I. Jonckheere *et al.*, "Review of methods for in situ leaf area index determination: Part I. Theories, sensors and hemispherical photography," *Agricultural and Forest Meteorology*, vol. 121, no. 1, pp. 19-35, 2004/01/20/ 2004, doi: https://doi.org/10.1016/j.agrformet.2003.08.027.

[85] W. G. M. Bastiaanssen, M. Menenti, R. A. Feddes, and A. A. M. Holtslag, "A remote sensing surface energy balance algorithm for land (SEBAL). 1. Formulation," *Journal of Hydrology*, vol. 212-213, pp. 198-212, 1998/12/01/ 1998, doi: https://doi.org/10.1016/S0022-1694(98)00253-4.

[86] G. C. Hulley, S. J. Hook, E. Abbott, N. Malakar, T. Islam, and M. Abrams, "The ASTER Global Emissivity Dataset (ASTER GED): Mapping Earth's emissivity at 100-meter spatial scale," *Geophysical Research Letters*, vol. 42, no. 19, pp. 7966-7976, 2015, doi: https://doi.org/10.1002/2015GL065564.

[87] M. Hori et al., "In-situ measured spectral directional emissivity of snow and ice in the 8–14 μm atmospheric window," *Remote Sensing of Environment*, vol. 100, no. 4, pp. 486-502,

2006/02/28/ 2006, doi: https://doi.org/10.1016/j.rse.2005.11.001.

[88] T. N. Carlson and D. A. Ripley, "On the relation between NDVI, fractional vegetation cover, and leaf area index," *Remote Sensing of Environment,* vol. 62, no. 3, pp. 241-252, 1997/12/01/ 1997, doi: https://doi.org/10.1016/S0034-4257(97)00104-1.

[89] J. A. Sobrino, J. C. Jiménez-Muñoz, and L. Paolini, "Land surface temperature retrieval from LANDSAT TM 5," *Remote Sensing of Environment,* vol. 90, no. 4, pp. 434-440, 2004/04/30/ 2004, doi: https://doi.org/10.1016/j.rse.2004.02.003.

[90] C. M. Beale, J. J. Lennon, J. M. Yearsley, M. J. Brewer, and D. A. Elston, “Regression analysis of spatial data,” *Ecol. Lett.*, vol. 13, no. 2, pp. 246–264, Feb. 2010.

[91] S. A. Ghausi, Y. Tian, E. Zehe, and A. Kleidon, “Radiative controls by clouds and thermodynamics shape surface temperatures and turbulent fluxes over land,” *Proc. Natl. Acad. Sci. USA*, vol. 120, no. 29, p. e2220400120, Jul. 18 2023.,

[92] J. Ma, H. Shen, P. Wu, J. Wu, M. Gao, and C. Meng, “Generating gapless land surface temperature with a high spatio-temporal resolution by fusing multi-source satellite-observed and model-simulated data,” *Remote Sens. Environ.*, vol. 278, p. 113083, 2022.

[93] F. Xu, J. Fan, C. Yang, J. Liu, and X. Zhang, “Reconstructing all-weather daytime land surface temperature based on energy balance considering the cloud radiative effect,” *Atmos. Res.*, vol. 279, p. 106397, 2022.

[94] D. J. Weiss, P. M. Atkinson, S. Bhatt, B. Mappin, S. I. Hay, and P. W. Gething, “An effective approach for gap-filling continental scale remotely sensed time-series,” *ISPRS J. Photogramm. Remote Sens.*, vol. 98, pp. 106–118, Dec. 2014.

[95] R. Yao, L. Wang, X. Huang, L. Sun, R. Chen, X. Wu, *et al.*, “A robust method for filling the gaps in MODIS and VIIRS land surface temperature data,” *IEEE Trans. Geosci. Remote Sens.*, vol. 59, no. 12, pp. 10738–10752, 2021.

[96] L. Görlitz, B. H. Menze, B. M. Kelm, and F. A. Hamprecht, "Processing spectral data," *Surface and Interface Analysis,* vol. 41, no. 8, pp. 636-644, 2009, doi: https://doi.org/10.1002/sia.3066.

[97] J. Holloway, K. J. Helmstedt, K. Mengersen, and M. Schmidt, "A Decision Tree Approach for Spatially Interpolating Missing Land Cover Data and Classifying Satellite Images," *Remote Sensing,* vol. 11, no. 15, p. 1796, 2019. [Online]. Available: https://www.mdpi.com/2072-4292/11/15/1796.

[98] S. E. Awan, M. Bennamoun, F. Sohel, F. Sanfilippo, and G. Dwivedi, "A reinforcement learning-based approach for imputing missing data," *Neural Computing and Applications,* vol. 34, no. 12, pp. 9701-9716, 2022/06/01 2022, doi: 10.1007/s00521-022-06958-3.

[99] A. Dumitrescu, M. Brabec, and S. Cheval, "Statistical Gap-Filling of SEVIRI Land Surface Temperature," *Remote Sensing,* vol. 12, no. 9, p. 1423, 2020. [Online]. Available: https://www.mdpi.com/2072-4292/12/9/1423.

[100] K. Rittger, K. J. Bormann, E. H. Bair, J. Dozier, and T. H. Painter, “Evaluation of VIIRS and MODIS snow cover fraction in high-mountain Asia using landsat 8 OLI,” *Front. Remote Sens.*, vol. 2, p. 647154, 2021.

[101] S. Strachan, E. P. Kelsey, R. F. Brown, S. Dascalu, F. Harris, G. Kent, *et al.*, “Filling the data gaps in mountain climate observatories through advanced technology, refined instrument siting, and a focus on gradients,” *Mt. Res. Dev.*, vol. 36, no. 4, pp. 518–527, 2016.

[102] H. Liu, N. Lu, H. Jiang, J. Qin, and L. Yao, “Filling gaps of monthly Terra/MODIS daytime land surface temperature using discrete cosine transform method,” *Remote Sens. (Basel)*, vol. 12, no. 3, p. 361, 2020.

[103] S. Luyssaert *et al.*, "Land management and land-cover change have impacts of similar magnitude on surface temperature," *Nature Climate Change,* vol. 4, no. 5, pp. 389-393, 2014/05/01 2014, doi: 10.1038/nclimate2196.

[104] P. K. Srivastava, D. Han, M. R. Ramirez, and T. Islam, "Machine Learning Techniques for Downscaling SMOS Satellite Soil Moisture Using MODIS Land Surface Temperature for Hydrological Application," *Water Resources Management*, vol. 27, no. 8, pp. 3127-3144, 2013/06/01 2013, doi: 10.1007/s11269-013-0337-9.

[105] M. Metz, V. Andreo, and M. Neteler, “A new fully gap-free time series of land surface temperature from MODIS LST data,” *Remote Sens. (Basel)*, vol. 9, no. 12, p. 1333, 2017.

[106] [104] Y. Xiao, W. Zhao, M. Ma, and K. He, “Gap-Free LST Generation for MODIS/Terra LST Product Using a Random Forest-Based Reconstruction Method,” *Remote Sens. (Basel)*, vol. 13, no. 14, p. 2828, 2021.

[107] S. Jäger, A. Allhorn, and F. Bießmann, “A benchmark for data imputation methods,” *Front. Big Data*, vol. 4, p. 693674, Jul. 8 2021.

[108] Q. Zhang, Q. Yuan, C. Zeng, X. Li, and Y. Wei, “Missing data reconstruction in remote sensing image with a unified spatial–temporal–spectral deep convolutional neural network,” *IEEE Trans. Geosci. Remote Sens.*, vol. 56, no. 8, pp. 4274–4288, 2018.

[109] P. Wu, Y. Su, S. Duan, X. Li, H. Yang, C. Zeng, *et al.*, “A two-step deep learning framework for mapping gapless all-weather land surface temperature using thermal infrared and passive microwave data,” *Remote Sens. Environ.*, vol. 277, p. 113070, 2022.

[110] W. Zhao and S.-B. Duan, “Reconstruction of daytime land surface temperatures under cloud-covered conditions using integrated MODIS/Terra land products and MSG geostationary satellite data,” *Remote Sens. Environ.*, vol. 247, p. 111931, 2020.

[111] M. Sarafanov, E. Kazakov, N. O. Nikitin, and A. V. Kalyuzhnaya, “A machine learning approach for remote sensing data gap-filling with open-source implementation: An example regarding land surface temperature, surface albedo and NDVI,” *Remote Sens. (Basel)*, vol. 12, no. 23, p. 3865, 2020.

[112] I. Buo, V. Sagris, and J. Jaagus, “Gap-filling satellite land surface temperature over heatwave periods with machine learning,” *IEEE Geosci. Remote Sens. Lett.*, vol. 19, pp. 1–5, 2021.

[113] D. Chen, Q. Zhuang, L. Zhu, W. Zhang, and T. Sun, “Generating Daily Gap-Free MODIS Land Surface Temperature Using the Random Forest Model and Similar Pixels Method,” *IEEE Access*, vol. 11,103274–103287, 2023.

[114] Y. Li, S. Zhu, Y. Luo, G. Zhang, and Y. Xu, “Reconstruction of Land Surface Temperature Derived from FY-4A AGRI Data Based on Two-Point Machine Learning Method,” *Remote Sens. (Basel)*, vol. 15, no. 21, p. 5179, 2023.

[115] X. Zhang, J. Zhou, S. Liang, L. Chai, D. Wang, and J. Liu, “Estimation of 1-km all-weather remotely sensed land surface temperature based on reconstructed spatial-seamless satellite passive microwave brightness temperature and thermal infrared data,” *ISPRS J. Photogramm. Remote Sens.*, vol. 167, pp. 321–344, 2020.

[116] J. Quan, Y. Guan, W. Zhan, T. Ma, D. Wang, and Z. Guo, “Generating 60–100 m, hourly, all-weather land surface temperatures based on the Landsat, ECOSTRESS, and reanalysis temperature combination (LERC),” *ISPRS J. Photogramm. Remote Sens.*, vol. 205, pp. 115–134, 2023.

[117] A. Jia, H. Ma, S. Liang, and D. Wang, “Cloudy-sky land surface temperature from VIIRS and MODIS satellite data using a surface energy balance-based method,” *Remote Sens. Environ.*, vol. 263, p. 112566, 2021.

[118] X. Zhang, W. Chen, Z. Chen, F. Yang, C. Meng, P. Gou, *et al.*, “Construction of cloud-free MODIS-like land surface temperatures coupled with a regional weather research and forecasting (WRF) model,” *Atmos. Environ.*, vol. 283, p. 119190, 2022.

[119] X. Zhang, J. Zhou, S. Liang, and D. Wang, “A practical reanalysis data and thermal infrared remote sensing data merging (RTM) method for reconstruction of a 1-km all-weather land surface temperature,” *Remote Sens. Environ.*, vol. 260, p. 112437, 2021.

[120] H. Zhang, B.-H. Tang, and Z.-L. Li, "A practical two-step framework for all-sky land surface temperature estimation," *Remote Sensing of Environment*, vol. 303, p. 113991,

2024/03/15/ 2024, doi: https://doi.org/10.1016/j.rse.2024.113991.

Seyedkarim Afsharipour received the M.Sc. degree in remote sensing and GIS from the Faculty of Geography, University of Tehran, Tehran, Iran, in 2018. He is currently pursuing the Ph.D. degree at the National Key Laboratory of Remote Sensing and Digital Earth, Aerospace Information Research Institute, Chinese Academy of Sciences, Beijing, China.

His research interests include earth observation data gap-filling and fusion, multi-sensor data integration, land surface analysis, and energy balance models. He is particularly focused on the development of advanced spatiotemporal fusion techniques to enhance the resolution and continuity of remote sensing observations. His work also involves analyzing surface energy fluxes, land-atmosphere interactions, and the impacts of environmental variability on land surface processes using remote sensing and geospatial modeling approaches.

Li Jia (Member, IEEE) received the B.S. degree in dynamic meteorology from the Beijing College of Meteorology, Beijing, China, in 1988, the M.Sc. degree in atmospheric physics from the Chinese Academy of Sciences, Beijing, in 1997, and the Ph.D. degree in environmental science from Wageningen University, Wageningen, The Netherlands, in 2004. She is currently a professor at the National Key Laboratory of Remote Sensing and Digital Earth, Aerospace Information Research Institute, Chinese Academy of Sciences, Beijing, China. Her research interests include the earth observation from ground-, airborne and spaceborne and its applications in hydrometeorology, water resource, agriculture and climate change. She developed the ETMonitor model based on satellite remote sensing observations for estimating evapotranspiration and generating multi-scale ET products. She is currently a member of the GEWEX-SSG (Global Energy and Water Exchanges Program - Scientific Steering Group), and a member of the GCOS-TOPC.

Massimo Menenti, received the Laurea degree in physics from the Università di Roma, Rome, Italy, in 1972, and the Ph.D. degree in environmental sciences from the Delft University of Technology, Delft, Netherlands. He has held senior research and faculty positions at Wageningen University, the International Institute for Geo-Information Science and Earth Observation (ITC), the National Research Council of Italy and the Delft University of Technology, The Netherlands.

He is currently a professor at the National Key Laboratory of Remote Sensing and Digital Earth, Aerospace Information Research Institute, Chinese Academy of Sciences, Beijing, China, at the Delft University of Technology, The Netherlands and a Research Director at the École Nationale Supérieure des Physique de Strasbourg (ENSPS), France.

His research interests include land surface processes, remote sensing of land-atmosphere interactions, surface energy balance modeling, and hydrological cycle analysis. He has made ground-breaking and early contributions to the development of remote sensing methodologies for water resource management, climate change studies, and land surface temperature retrieval. His research integrates multi-source satellite observations with numerical models to improve environmental monitoring and prediction.

Prof. Menenti is a Fellow of IEEE and has served as an editor and reviewer for multiple geoscience and remote sensing journals. He has played a key role in various international research collaborations, including projects with ESA, NASA, and the European Union, focusing on earth observation, climate change, and hydrological modeling.